# Retroviral Infection of Human Neurospheres and Use of Stem Cell EVs to Repair Cellular Damage

**Heather Branscome[1, 2], Dezhong Yin[3], Sheela Jacob[3], Maria Cowen[1], Yuriy Kim[1], Pooja Khatkar[1], James Erickson[1], Nazira El-Hage[4], Lance A. Liotta[5] and Fatah Kashanchi[1*]**

[1] Laboratory of Molecular Virology, School of Systems Biology, George Mason University, Manassas, VA.

[2] American Type Culture Collection (ATCC), Manassas, VA.

[3]ATCC Cell Systems, Gaithersburg, MD.

[4]Department of Immunology and Nano-Medicine, Herbert Wertheim College of Medicine, Florida International University, Miami, FL.

[5]Center for Applied Proteomics and Molecular Medicine, George Mason University, Manassas, VA.

*** Correspondence:** Fatah Kashanchi, Ph.D., Laboratory of Molecular Virology, George Mason University, Discovery Hall Room 182, 10900 University Blvd., Manassas, VA 20110. Tel.: 703-993-9160, Fax: 703-993-7022. Email: fkashanc@gmu.edu

**Abstract**

HIV-1 remains an incurable infection that is associated with substantial economic and epidemiologic impacts. HIV-associated neurocognitive disorders (HAND) are commonly linked with HIV-1 infection; despite the development of combination antiretroviral therapy (cART), HAND is still reported to affect at least 50% of HIV-1 infected individuals. It is believed that the over-amplification of inflammatory pathways, along with release of toxic viral proteins from infected cells, are primarily responsible for the neurological damage that is observed in HAND; however, the underlying mechanisms are not well-defined. Therefore, there is an unmet need to develop more physiologically relevant and reliable platforms for studying these pathologies. In recent years, neurospheres derived from induced pluripotent stem cells (iPSCs) have been utilized to model the effects of different neurotropic viruses. Here, we report the generation of neurospheres from iPSC-derived neural progenitor cells (NPCs). We show, for what we believed to be the first time, that these cultures are susceptible to retroviral (e.g. HIV-1, HTLV-1) infection. In addition, we also examine the functional effects of stem cell derived extracellular vesicles (EVs) on HIV-1 damaged cells as there is abundant literature supporting the reparative and regenerative properties of stem cell EVs in the context of various CNS pathologies. Consistent with the literature, our data suggests that stem cell EVs may modulate neuroprotective and anti-inflammatory properties in damaged cells. Collectively, this study demonstrates the feasibility of NPC-derived neurospheres for modeling HIV-1 infection and, subsequently, highlights the potential of stem cell EVs for rescuing cellular damage induced by HIV-1 infection.

**Keywords**: Neurospheres, neural progenitor cells (NPCs), HIV-1, stem cells, extracellular vesicles (EVs)

52 **Introduction**

53 HIV-1 remains an incurable infection and as of 2018 approximately 37.9 million people were estimated to
54 be living with HIV-1, with an average of 1.7 million new infections occurring annually [1]. In addition to its
55 deleterious impact on the immune system, HIV-1 also contributes to neurocognitive impairments. HIV-associated
56 neurocognitive disorders (HAND) are commonly associated with HIV-1 infection and comprise a range of
57 neurological dysfunctions, including asymptomatic neurocognitive impairment, mild neurocognitive disorder, and
58 HIV-associated dementia [2]. Despite the development of combination antiretroviral therapy (cART), which
59 effectively suppresses viral replication and has vastly improved the quality of life for those treated, HAND is still
60 reported to affect up to 50% of infected individuals [3,4]. Therefore, HAND represents a considerable cause of
61 morbidity in these populations.

62 Although the exact mechanisms that contribute to its persistence are poorly understood, it is believed that
63 the over-amplification of inflammatory pathways, along with the release of toxic viral proteins from infected cells,
64 are primarily responsible for the neurological damage that is observed in HAND [5,6,7,8]. While neurons are not
65 directly infected by HIV-1, they remain highly susceptible to the cellular damage and injury mediated by viral
66 proteins such as gp120 and Tat. Additionally, the release of pro-inflammatory cytokines, including TNF-α, IL-1β
67 and IL-6, from infected macrophages and microglia can also promote neuronal damage and neuronal apoptosis and
68 it has also been suggested that exposure of astrocytes to these factors can further exacerbate neurotoxic effects [5,6].
69 Consequently, there is a gap of knowledge surrounding the neuropathology of HAND and the mechanisms that
70 contribute to its persistence.

71 The complexity of the Central Nervous System (CNS) relative to other systems in the body has largely
72 limited the progress of CNS disease modeling and drug development. Moreover, the global incidence of CNS
73 diseases, including neurocognitive and neurodegenerative disorders as well as neurological infections, has
74 substantially risen throughout the last several decades. This, in turn, imposes a substantial socioeconomic burden.
75 For example, a recent report found that approximately 16.5% of global deaths are caused by neurological diseases
76 and the estimated costs associated with these diseases are expected to range from $600 to $700 million [9, 10]. This
77 underscores the outstanding need for the development of novel research platforms which can allow for improved
78 modeling of CNS pathologies, including those related to HIV-1 infection.

79 Improvements in biotechnology, coupled with progress in stem cell research, have revolutionized the

80 biomedical field during the last decade. Specifically, induced pluripotent stem cells (iPSCs) represent a relatively
81 novel platform that has allowed for advanced disease modeling and drug discovery [11]. Using this technology,
82 adult somatic cells can be reprogrammed into an embryonic-like state via the overexpression of transcription factors
83 (e.g. Oct3/4, SOX2, c-Myc, Klf4) responsible for maintaining pluripotency. Takahashi and Yamanaka first
84 demonstrated this in 2006 with the successful reprogramming of mouse somatic cells into iPSCs and again, in 2007,
85 when they generated iPSCs from human fibroblasts [12, 13]. In the context of the CNS, iPSCs have the potential to
86 differentiate into a wide variety of neuronal and glial cell types including dopaminergic, cortical, and motor neurons
87 as well as astrocytes, oligodendrocytes, microglia, and neural precursors [14, 15, 16, 17]. Along these lines, iPSCs
88 have been employed to model a number of different CNS pathologies ranging from Alzheimer's, Parkinson's, and
89 Huntington's disease, to amyotrophic lateral sclerosis, multiple system atrophy, and Zika, West Nile virus, and HIV-
90 1 [18, 19, 20, 21, 22, 23, 24, 25].

91 In recent years, human iPSCs have been used to derive neural stem cells (NSCs) and/or neural progenitor
92 cells (NPCs); these neuronal cultures have subsequently been used to efficiently generate three-dimensional (3D)
93 neurospheres *in vitro*. In general, 3D models are expected to be superior to traditional 2D culture models of NPCs
94 due to their resemblance to the *in vivo* cellular environment which permits a more accurate representation of tissue-
95 specific architecture and cell to cell communication [26,27,28]. Along these lines, it has been demonstrated that
96 NPC-derived neurospheres are similar to those derived from primary fetal human NPCs with respect to migration,
97 proliferation, and differentiation [29]. Additionally, it has previously been shown that neurospheres partially
98 maintain regionally specific expression of developmental control genes *in vitro* and, moreover, that cells derived
99 from these spheres retain the ability to differentiate into cellular subtypes representative of their regional origin [30,
100 31, 32]. Therefore, the use of 3D neurospheres is expected to serve as a complementary approach to *in vivo* studies
101 relating to neurogenesis and neural development.

102 More recently, others have employed the use of 3D neurospheres to model the effects of different
103 neurotropic viruses. For example, Garcez et al. investigated the consequences of Zika virus (ZIKV) infection and
104 found that human iPSC-derived neurospheres exposed to ZIKV exhibited morphological abnormalities and had a
105 higher induction of apoptosis relative to mock infection [33]. In a follow-up study which included proteomic and
106 mRNA transcriptional profiling of infected neurospheres, these authors generated further data suggesting that ZIKV
107 impaired pathways related to cell cycle and neuronal differentiation [34]. Additionally, D'Aiuto et al. utilized

108 human iPSCs to generate 3D neurospheres to evaluate herpes simplex virus type 1 (HSV-1) infection [35]. The
109 results from these studies demonstrated that neurospheres remained viable after four weeks in culture, were capable
110 of differentiating into not only mature neurons (glutamatergic, GABAergic, dopaminergic) but also glial cells, and
111 could be applied in a high throughput fashion for drug screening. Taken together, this research strongly suggests
112 that neurospheres are physiologically relevant models that can be used to study not only the cellular and molecular
113 interactions in both healthy and diseased states but can also serve as a reliable platform for drug testing.
114 Furthermore, they set an essential precedent for the modeling of other neurotropic viruses.

115 As described earlier, the development of CNS therapeutics has met relatively limited success. Factors
116 relating to overall disease complexity, lengthy developmental periods and stringent regulatory review, coupled with
117 the challenge of drug delivery across the blood-brain-barrier (BBB) have hindered progress in this field [36, 37].
118 While stem cell therapy has been studied in the context of CNS pathologies, there is now an emerging interest in the
119 potential therapeutic application of stem cell-derived extracellular vesicles (EVs) as these vesicles have been shown
120 to mediate many of the reparative and regenerative properties associated with their donor stem cells [38]. Briefly,
121 EVs are nano-sized vesicles that are generally classified by their size and biogenesis. Two of the most widely
122 studied subtypes of EVs are exosomes, which range approximately 50 to 150 nm in size and originate from the
123 endosome, and microvesicles (MVs), which range approximately 50 to 1000 nm in size and are released directly
124 from the plasma membrane [39]. EVs are enriched with a diverse array of biological cargo which includes RNAs,
125 proteins, cytokines, and lipids and this cargo is believed to drive EV potency [40, 41]. Accordingly, EVs from both
126 mesenchymal stem cells (MSCs) and iPSCs have been broadly studied for their functional effects and there is rich
127 literature to support their potential therapeutic application in various pathologies as reviewed elsewhere [42, 43].

128 With respect to the CNS, there is accumulating evidence which strongly indicates that stem cell EVs exert
129 both immunomodulatory and neuroprotective effects to promote functional recovery in damaged tissue [44, 45, 46,
130 47]. However, it is important to note that this field is still in its infancy. Moreover, whether stem cell EVs may
131 confer beneficial effects in the context of CNS infection, including HIV-1 and HAND, remains to be addressed.
132 Thus, studies of this nature are imperative to better characterize the potential neuroprotective properties of stem cell
133 EVs and to determine the mechanisms by which these EVs may repair cellular damage that is induced by different
134 viral infections.

135 Here, we report the generation of neurospheres from NPCs derived from normal human iPSCs. These

136 cultures not only exhibit reproducibility with respect to morphology and size but also demonstrate the ability to be
137 stably maintained in culture to permit differentiation into different CNS cell types. Importantly, we show, for what
138 we believe to be the first time, that these cultures are permissive to HIV-1 infection using three different viral
139 isolates. We also include data to show that neurospheres co-cultured with HTLV-1 infected cells may also be
140 susceptible to HTLV-1 infection. Lastly, we evaluate the potential reparative effects of both MSC and iPSC EVs on
141 HIV-1 damaged cells in both 2D cultures and 3D neurospheres. Collectively, this data highlights NPC-derived
142 neurospheres as relevant and robust models for future studies relating to HIV-1 infection and HAND and,
143 subsequently, demonstrates the potential application of stem cell EVs for rescuing cellular damage induced by HIV-
144 1 infection.

145

146
147
148
149
150
151
152
153
154
155
156
157
158
159
160
161
162
163
164
165

166 **Results**

167 **Generation and Characterization of NPC-derived Neurospheres**

168 The ability of NPCs to aggregate and assembly into physiologically relevant 3D structures that are also
169 permissive to viral infection, namely Zika and HSV-1 infection, has recently been published by others [27, 33, 34,
170 35,48]. To further expand upon these studies, we were interested in evaluating the susceptibility of NPC-derived
171 neurospheres to retroviral infection. For these studies we utilized commercially available NPCs that had been
172 established from normal human iPSCs. The diagram in Fig. 1a summarizes the overall workflow and timeline
173 associated with the generation of NPCs and neurospheres. Briefly, adult somatic cells were directly reprogrammed
174 into iPSCs using a non-integrating Sendai-based reprogramming kit following established protocols [49]. To
175 authenticate the quality of iPSCs, their germ line differentiation potential was confirmed by pluripotency testing
176 (PluriTest); furthermore, flow cytometry confirmed positive expression (>85%) of stem cell markers SSEA4 and
177 TRA-1-60 and negative expression (<15%) of SSEA-1. iPSCs then underwent embryoid body (EB) formation to
178 assemble into spherical colonies that were subsequently differentiated into NPCs. NPCs were briefly scaled up in
179 2D culture prior to the induction of neurosphere formation.

180 In an effort to promote the controlled and consistent formation of neurospheres, NPCs were seeded at a
181 high density in individual U-shaped wells of an ultra-low attachment 96-well plate. After 24 to 48 hours of
182 incubation a single, well-defined neurosphere was visible in each well. Representative phase contrast images in Fig.
183 1b show that this methodology resulted in uniformly shaped spheres that maintained their morphology and structure
184 throughout the differentiation process (weeks 12 through 14). Using calibrated imaging software, the average
185 diameter of each sphere in Fig. 1b was measured and graphed. As shown in Fig. 1c, the average diameter of the
186 neurospheres remained between 700 to 800 μm. This quantitative analysis indicates that NPC-derived neurospheres
187 maintain a relatively consistent size over time and, moreover, demonstrates the reproducibility of our protocols.

188 The NPCs used in these experiments were previously authenticated via immunocytochemistry (ICC) for
189 expression of the neural stem cell (NSC) markers Nestin and Pax6 in 2D cultures. Additionally, these NPCs have
190 displayed robust expression of the early neuronal marker Tuj1, the dopaminergic marker tyrosine hydroxylase (TH),
191 and astrocytic marker GFAP when cultured in the appropriate differentiation medium (Supplementary Fig. 1). This
192 data is consistent with the reports of others who have shown that NPCs are capable of differentiating into not only
193 mature neurons but also glial cells [50, 51, 52, 53, 54]. Given these results, we rationalized that NPC-derived

194 neurospheres would retain their inherent differentiation capacity in 3D culture. ICC staining of neurospheres that
195 had been cultured in differentiation medium for two weeks indicated a mixed population of cells which included
196 dopaminergic neurons (FOXA2$^+$), astrocytes (GFAP$^+$), and microglia-like cells (CD163$^+$). Data in Fig. 1d shows
197 that FOXA2 expression appeared relatively diffuse and uniformly distributed, GFAP expression appeared more
198 localized towards the periphery, and CD163 expression appeared relatively sparse throughout the sphere. Staining
199 for Iba-1 also revealed weak expression, suggesting the absence of activated microglia. Collectively, this data
200 highlights the ability of iPSC-derived NPCs to self-assemble into neurospheres that maintain their ability to
201 differentiate into both neurons and glial-like cells.

202 **Infection of Neurospheres**

203 We next sought to assess the susceptibility of NPC-derived neurospheres to HIV-1 infection. For these
204 experiments, neurospheres were cultured in the presence of HIV-1 dual tropic 89.6 (MOI:10). In addition, since
205 HIV-1 infected individuals utilize combined antiretroviral therapy (cART), neurospheres were also treated with a
206 cocktail consisting of equal parts lamivudine, tenofovir disoproxil fumarate, emtricitabine, and indinavir to model
207 the effects of cART [1]. After seven days in culture, supernatants were collected and neurospheres were harvested
208 for downstream assays. To determine whether exposure of neurospheres to HIV-1 resulted in effective viral
209 replication, total cellular protein was isolated and western blot was performed to assess the expression of different
210 viral proteins. As shown in Fig. 2a, p24 capsid protein, uncleaved Gag polyprotein Pr55, and accessory protein Nef
211 were all detected in neurospheres exposed to HIV-1 89.6. The cART cocktail used for these experiments consisted
212 of a mixture of nucleoside reverse transcriptase inhibitors (NRTIs) and a protease inhibitor; as expected, culturing of
213 neurospheres with cART reduced the expression of p24, Pr55, and Nef to almost undetectable levels. RT-qPCR for
214 HIV-1 TAR and *env* confirmed the presence of these RNAs in HIV-1 89.6-exposed neurospheres with
215 approximately $10^5$ and $10^4$ copies being detected, respectively, relative to the control (uninfected) neurospheres (Fig.
216 2b). Here, treatment with cART also resulted in decreased expression of both TAR and *env* RNA.

217 To validate these results, we also exposed neurospheres to two other HIV-1 lab adapted strains, JR-CSF
218 (MOI:10) and CHO40 (MOI:10) with or without cART. After seven days in culture, supernatants were collected
219 and neurospheres were harvested for downstream assays. Total cellular proteins were isolated and, again, western
220 blot showed the presence of p24 capsid protein in neurospheres exposed to each viral isolate (Fig. 2c). Moreover,
221 the level of p24 expression appeared relatively consistent among 89.6, JR-CSF, and CHO40-exposed neurospheres.

222 Collectively, this data shows that HIV-1 viral replication occurs in NPC-derived neurospheres in a reproducible
223 manner.

224 We were also interested in examining the potential tropism of HIV-1 in neurospheres. While CD4+T cells
225 are the most abundantly HIV-1 infected cells in the body there is ample evidence to suggest that microglia and
226 astrocytes are not only capable of being infected by HIV-1, but may also serve as viral reservoirs, as reported
227 elsewhere [55, 56, 57, 58, 59, 60, 61]. NPCs were gently disaggregated with trypsin and immunoprecipitation (IP)
228 was performed using antibodies for either astrocytes ($GFAP^+$), microglia-like cells (Integrin αm/$CD11b^+$), mature
229 neurons ($GAD65^+$), or NSCs ($SOX2^+$). We next performed direct PCR of the IP material without purification of
230 DNA as RNA isolation from a relatively small number of infected cells would not yield a sufficient amount for RT-
231 qPCR. Results from qPCR confirmed the presence of TAR DNA in microglia-like cells in the 89.6, JR-CSF, and
232 CHO40 infected neurospheres (Fig. 2d). While the highest numbers of TAR DNA were associated with astrocytes
233 (~480 copies) and microglia-like cells (~780 copies) in the JR-CSF samples, lower amounts were also detected in
234 microglia-like cells from the 89.6 (~ 114 copies) and CHO40 (~ 125 copies) samples. In addition, astrocytes from
235 the JR-CSF-infected neurospheres (~480 copies) had substantially higher levels of TAR DNA than astrocytes from
236 the 89.6 and CHO40-infected neurospheres (< 20 copies each). However, within the JR-CSF samples, TAR DNA
237 was still the most abundant in microglia-like cells. Consistent with the literature, this data suggests that HIV-1
238 tropism in neurospheres is directed towards glial cells [55, 56, 57, 58, 59, 60, 61].

239 Based on these findings, we next sought to assess the potential effects of HIV-1 (89.6) on the expression
240 levels of multiple proteins or enzymes associated with different CNS cell types. To this end, western blot was
241 performed to evaluate the relative expression microglia-like cells ($CD11b^+$, $CD163^+$), astrocytes ($GFAP^+$, glutamine
242 synthetase$^+$), dopaminergic neurons ($TH^+$, $FOXA2^+$), GABAergic neurons ($GAD65^+$, $GAD67^+$), glutamatergic
243 neurons ($BNPI^+$) and NSCs ($SOX2^+$). As shown in Fig. 3a, HIV-1 appeared to increase the expression of
244 differentiated neurons, particularly $TH^+$, $GAD65^+$/$GAD67^+$, and $BNPI^+$ neurons, whereas treatment with cART
245 reduced the expression of these markers to levels that were comparable to the uninfected sample. A similar pattern
246 of expression was also observed for GFAP, while the expression of CD11b appeared relatively consistent between
247 the uninfected, HIV-1 infected, and cART samples.

248 As an additional control, we also evaluated the effects of co-culturing neurospheres with the HTLV-1
249 infected cell line HUT 102. HTLV-1 is the etiologic agent of HTLV-1-associated myelopathy/tropical spastic

250 paraparesis (HAM/TSP), a neurological disorder that is characterized by chronic neuroinflammation and
251 neurodegeneration [62, 63, 64, 65]. Prior to initiating the co-culture, HUT 102 cells were exposed to ionizing
252 radiation (IR) to inhibit chromosomal replication and to activate viral transcription, as previously described [66, 67,
253 68]. Treatment with a combination of IFN/AZT was also included to model the current standard for HTLV-1 anti-
254 viral therapy [69, 70, 71]. The irradiated HUT 102 cells served as the background control. After seven days of co-
255 culture, neurospheres were harvested for downstream assays. Data in Fig. 3a shows that HTLV-1 co-culture
256 resulted in a slight increase in the expression of FOXA2 and BNPI neurons and that treatment with IFN/AZT
257 reversed this increase. On the other hand, HTLV-1 appeared to reduce the expression of both CD11b and glutamine
258 synthetase relative to the uninfected sample, whereas IFN/AZT did not appear to have any impact. While the
259 expression of NSCs appeared relatively faint in the uninfected and HIV-1 samples, its expression was undetectable
260 in the HTLV-1 samples. These results are not entirely surprising as neurospheres were cultured in medium that was
261 enriched to induce differentiation into more mature cell types.

262 To confirm whether HTLV-1 was capable of replicating in neurospheres, western blot was performed to
263 assess the expression of HTLV-1 Tax and matrix (p19) proteins. As shown in Fig. 3b, the expression of both Tax
264 and p19 was higher after co-culturing of neurospheres with irradiated HUT 102 cells (relative to the background
265 control), thereby indicative of viral replication. As expected, treatment with IFN/AZT reduced the expression of
266 Tax and p19 to levels that were similar to the background control. Furthermore, RT-qPCR for HTLV-1 *tax*, *env,*
267 and *hbz* RNA showed that the expression of *tax* and *env* increased after co-culture and that treatment with IFN/AZT
268 resulted in a considerable reduction of *tax* and *env* transcripts. This expression pattern was also observed among
269 *hbz*, although to a much lower effect (Fig. 3c).

270 Overall, these results demonstrate the ability of HIV-1 to replicate in NPC-derived neurospheres, therefore
271 indicating that these models may be permissive to infection. While the primary focus of this manuscript remains on
272 HIV-1, the data generated from the HTLV-1 experiments confirms the susceptibility of neurospheres to retroviral
273 infection and lays the foundation for future experiments focused on HTLV-1 or other retroviral infections. Lastly,
274 this data also points towards the differential effects of viral infection on the cellular composition of neurospheres.
275 Since neurospheres are composed of a heterogeneous population of cell types, including those that are infected and
276 uninfected, this area of research deserves further attention.

277 **The Effect of Stem Cell EVs on HIV-1 Infected Neurospheres**

278 Our experiments have shown receptor mediated alterations post-infection, indicating cellular damage.
279 Therefore, there is a need for a "holistic" reparative approach to potentially control cellular damage and regulate
280 inflammation. There is mounting evidence that EVs from different sources of stem cells, namely MSCs and iPSCs,
281 possess broad reparative and regenerative properties across various pathologies, including those related to the CNS
282 [42, 43, 44, 45, 46, 47]. Whether or not these vesicles confer reparative effects in the context of infection remains
283 relatively unexplored, especially with respect to the CNS. Our previous research pointed towards the potential
284 reparative effects of both MSC and iPSC EVs in 2D cultures of neurons, astrocytes, and monocyte-derived
285 macrophages (MDMs) damaged by IR [72]. Therefore, we sought to expand upon these studies by investigating the
286 potential functional effects of MSC and iPSC EVs in HIV-1 infected neurospheres.

287 The EVs used for these experiments were isolated using a scalable platform which incorporated the use of
288 tangential flow filtration (TFF) [72]. This advanced technology has the ability to produce large batches of highly
289 concentrated material in an efficient and reproducible manner and in recent years it's application for EV isolation
290 has been well documented by others [73, 74, 75, 76]. Here, we include data from the analysis of MSC and iPSC
291 EVs; we also include data from A549 (cancer) EVs which served as a control for our EV isolation method and EV
292 uptake assay. NTA analysis of each EV preparation showed that the majority of vesicles fall within 50 to 150 nm in
293 diameter, which is consistent with the size of exosomes (Fig. 4a). Specifically, iPSC and MSC EVs displayed mode
294 (peak) diameters of 97 nm and 76 nm, respectively, while A549 EVs displayed a slightly higher mode diameter of
295 138 nm. Moreover, both iPSC and MSC EVs also exhibited prominent secondary peaks at 144 nm and 128 nm,
296 respectively, while A549 EVs showed a relatively heterogeneous size distribution.

297 To assess the efficiency of their uptake by neurospheres, EVs were fluorescently labeled with the nonpolar
298 dye BODIPY which stains neutral and nonpolar lipids. Labeled EVs were then added to cultures of differentiated
299 neurospheres. As shown in Fig. 4b, fluorescent microscopy initially revealed a relatively weak signal that persisted
300 throughout the first 24 hours (day 1). However; over time, the fluorescent intensity increased and representative
301 photographs (day 8) show a strong fluorescent signal that is predominantly localized in the center of each EV-treated
302 neurosphere. We also obtained similar results when using the SYTO® RNASelect™ nucleic acid stain to label
303 EVs. Here, a strong fluorescent signal was observed around the periphery of each neurosphere 8 days after EV
304 treatment (Supplementary Fig. 2a).

305 Interestingly, we also observed that neurospheres treated with iPSC and A549 EVs displayed a change in
306 morphology that was characterized by a reduction in their well-defined spherical structure relative to the MSC EV-
307 treated neurosphere (day 8). This prompted us to question whether iPSC and A549 EVs may contain enzymes
308 capable of degrading the extracellular matrix within neurospheres. To address this, we performed western blot for
309 matrix metalloproteinase 9 (MMP9), as it is one of the most well-studied members of the MMP family and,
310 interestingly, has also been associated with reparative and regenerative functions in the CNS [77, 78]. Results from
311 this experiment revealed MMP9 expression in both iPSC and A549 EVs, while its expression was undetected in
312 MSC EVs (Supplementary Fig. 2b). As a follow-up, we performed gelatin zymography, as this is a reliable assay to
313 assess the relative proteolytic activity of experimental samples [79, 80]. Imaging of the stained gel indicated the
314 presence of active MMP9 as well as active MMP2 in each EV prep. Among the samples A549 EVs displayed the
315 highest intensity, followed by iPSC and MSC EVs (Supplementary Fig. 2c). This data suggests that EVs are capable
316 of not only penetrating, but also persisting in, three-dimensional cultures and, moreover, that EV-associated
317 proteolytic enzymes may partially contribute to this effect.
318 After confirming EV uptake by neurospheres we shifted our focus to next examine their potential
319 functional effects in HIV-1 infected neurospheres. To date, the anti-apoptotic effects of stem cell EVs in the context
320 of the CNS have been well documented both *in vitro* and *in vivo* [81, 82, 83, 84, 85, 86]. To this end, we performed
321 western blot to examine the expression levels of different proteins involved in the regulation of apoptosis (Fig. 4c).
322 Relative to the uninfected control sample, HIV-1 was associated with a slight increase in the expression of cleaved
323 PARP-1. The expression of p53 was lower in HIV-1 neurospheres and the expression of phosphorylated p53 at
324 serine 15 (p-p53) was increased, indicative of increased DNA binding to regulate G1/S and G2/M checkpoints.
325 Additionally, the expression of phosphorylated p21 at serine 146 (p-p21) was decreased, potentially indicating a
326 reversal of cyclin-dependent kinase inhibition. The addition of cART alone did not appear to have an effect on the
327 expression of cleaved PARP-1, p53, or p-p53; however, cART slightly increased the expression of p-p21 relative to
328 the HIV-1 infected sample. On the other hand, the addition of cART combined with either iPSC or MSC EVs
329 appeared to restore expression of cleaved PARP-1, p53, p-p53, and p-p21 to levels comparable to the control.
330 Interestingly, the expression level of cleaved caspase-3 remained low and relatively undetectable among each
331 sample (Fig. 4c).
332 In addition to their anti-apoptotic effects, stem cell EVs are also associated with potent anti-inflammatory

333 properties and several recent studies have highlighted their ability to reduce neuroinflammation in various models of
334 CNS damage [87, 88, 89, 90, 91, 92]. To assess the potential anti-inflammatory effects of stem cell EVs on HIV-1
335 infected neurospheres, we performed western blot for well-known pro-inflammatory mediators (Fig. 4d). Here,
336 substantial increases in TNFα, IL-8, and IL-1β were observed after HIV-1 infection. Treatment with cART
337 decreased expression of soluble IL-1β to an undetectable level while only slightly decreasing the expression of
338 TNFα and IL-8. Notably, similar results were also observed in JR-CSF and CHO40-infected neurospheres
339 (Supplementary Fig. 3). Again, in HIV-1 89.6-infected neurospheres, the combination of cART with either iPSC or
340 MSC EVs restored the expression of TNFα, IL-8 and IL-1β to levels that were comparable to the uninfected control.
341 Taken together, this data indicates that both iPSC and MSC EVs are capable of exerting both neuroprotective and
342 anti-inflammatory effects in HIV-1 infected neurospheres.

343 **RNA Analysis of Stem Cell EVs**

344 The reparative aspects of stem cell EVs have been shown to be associated with various non-coding RNAs
345 and/or proteins that confer protective and/or immunomodulatory functions in damaged recipient cells [93, 94, 95,
346 96, 97]. While several recent studies have extensively characterized the miRNA profiles of stem cell EVs, the
347 characterization of EV-associated long non-coding RNAs (lncRNAs) remains a relatively unexplored topic [98, 99,
348 100, 101]. Our previous studies included the sequencing of lncRNAs (≥ 250 base pairs) from iPSC, MSC, and A549
349 EVs [72]. Again, the purpose of including A549 EVs was to serve as a non-stem cell control. Here, we share an
350 expanded set of data to highlight the differences that exist among these different EV populations.

351 Overall, approximately 6.5 x$10^7$, 1.9 x $10^7$, and 2.6 x $10^7$ valid reads were obtained from iPSC, MSC, and
352 A549 EVs, respectively, with each preparation having a Q30 score greater than 85% (Supplementary Table 1). Of
353 these reads, approximately 80.88% (iPSC), 71.21% (MSC), and 70.66 (A549) were mapped to the genome. As
354 shown in Fig. 5a, the majority of lncRNAs among each EV preparation mapped to introns. iPSC EVs had the
355 highest number of intronic transcripts (93%) followed by MSC EVs (79%) and A549 EVs (75%). The percentage of
356 transcripts mapping to either exons or intergenic regions ranged from approximately 10 to 15% among MSC and
357 A549 EVs; however only ~3% of transcripts from iPSC EVs were mapped to these regions. The chromosome maps
358 of EV-associated lncRNA transcripts revealed striking differences in the density distribution when comparing stem
359 cell EVs and A549 EVs. Specifically, transcripts from A549 EVs appeared more evenly distributed and spanned all
360 chromosomes while transcripts from iPSC and MSC EVs only mapped to certain chromosomal regions (Fig. 5b).

361 Transcripts that were not annotated in genome annotation databases were subsequently designated as novel
362 transcripts according to the following class codes: i = transfrag falling within a reference intron; j = potentially novel
363 isoform with at least one splice junction shared with a reference transcript; o = generic exonic overlap with a
364 reference transcript; u = unknown intergenic transcript; x = exonic overlap with reference on the opposite strand.
365 Data in Fig. 5c shows that within each EV prep, the majority of transcripts either fell within a reference intron (i)
366 (> 50%) or were classified as unknown intergenic transcripts (u) (< 40%) and, moreover, that ≤ 0.1% of transcripts
367 among each sample were classified as either "j", "o", or "x".
368 Heat maps generated from all EV-associated lncRNA transcripts show the comparisons between iPSC and
369 A549 EVs (Fig. 5d, left panel) and between MSC and A549 EVs (Fig. 5d, right panel). Additionally, volcano plots
370 in Fig. 5e provide a visual representation of the differentially expressed transcripts between iPSC and A549 EVs
371 (Fig. 5e, left panel) and between MSC and A549 EVs (Fig. 5e, right panel). Transcripts displaying statistically
372 significant regulation (either up or down) are annotated with their associated gene ID/transcript name. Overall,
373 these plots reveal that a majority of transcripts associated with stem cell EVs are downregulated relative to A549
374 EVs. Additionally, iPSC EVs displayed a greater amount of significantly up-regulated transcripts relative to MSC
375 EVs when compared to A549 EVs. Notably, transcript MSTRG.106597 was among the most significantly
376 upregulated transcript associated with both iPSC EVs and MSC EVs and its approximate fold change relative to
377 A549 EVs was 3392 for iPSC EVs and 229 for MSC EVs. For reference, this is designated as a novel transcript
378 which corresponds to gene FP671120.1. Supplementary Fig. 4 includes a comparison of the lncRNA transcripts
379 between iPSC and MSC EVs. While the corresponding volcano plot shows a relatively even distribution of up- and
380 down-regulated transcripts, iPSC EVs are associated with a few significantly regulated transcripts.
381 Annotated transcripts were further analyzed by performing Gene ontology (GO) (Supplementary Fig. 5).
382 Relative to A549 EVs, iPSC EVs had significantly enriched GO terms which included RNA and protein binding,
383 positive regulation of GTPase activity and cell adhesion. Relative to A549 EVs, MSC EVs had significantly
384 enriched GO terms which included RNA binding, protein binding, and T cell receptor signaling pathway.
385 Collectively, this data reveals distinct differences in the expression of lncRNA transcripts associated with EVs
386 derived from stem cells versus cancer (A549) cells. Future studies will include a more thorough assessment of the
387 differentially expressed transcripts among iPSC and MSC EVs and will focus on their potential functional
388 implications.

389 **Detection of RNA Binding Proteins Using RNA Pull-down Assay**

390 In an effort to define the role of EV-associated lncRNAs and to better understand their potential functional
391 significance in recipient cells, we recently identified at least one lncRNA transcript associated with iPSC EVs
392 (AC120498.9) which possessed a unique secondary structure [72]. Specifically, this transcript contained two
393 continuous stretches of double-stranded RNA that were greater than 30 base pairs (bp) in length, a property that has
394 previously been associated with the activation of PKR [102, 103]. This prompted us to further examine the
395 secondary structures of other EV-associated lncRNAs, first by focusing on those that were more highly associated
396 with iPSC EVs. We subsequently generated secondary structures from over 240 iPSC EV-associated lncRNAs that
397 had FPKM values of ≥ 2 relative to MSC and A549 EVs. From this analysis we identified another transcript
398 (ADIRF-AS1) which also contained a continuous stretch of double-stranded RNA greater than 30 bp. For reference,
399 the secondary structures of ADIRF-AS1 and AC120498.9 are shown in Fig. 6a.

400 To assess whether the identified sequences were capable of binding to PKR in neurons, the biotin-
401 conjugated synthetic RNA sequences were incubated with whole cell lysate and then purified using Streptavidin-
402 Sepharose beads. Western blot was performed to assess the expression of PKR, as well as other critical RNA
403 binding proteins. The results in Fig. 6b confirm that the relevant sequences from both ADIRF-AS1 and
404 AC120498.9 were capable of binding not only to PKR, but also to other double stranded RNA (dsRNA) binding
405 proteins including DICER and ADAR1. We additionally performed similar experiments using whole cell lysate
406 from either astrocytes or MDMs (Supplementary Fig. 6). Again, western blot analysis confirmed expression of
407 PKR, DICER, and RIG-I, thereby highlighting the potential of these RNAs to bind to multiple different RNA
408 binding proteins in CNS relevant cell types. As a negative control for these experiments, we did not detect
409 expression of p65 (data not shown). Collectively, we suspect that these innate immune molecules may bind to EV-
410 associated lncRNAs to either activate their enzymatic activities or, alternatively, to suppress their functions in
411 recipient cells. Future studies will better focus on the potential significance of this binding.

412 **Stem Cell EVs Rescue Cellular Viability in HIV-1 Damaged Neurons**

413 Based on the above data showing that NPC-derived neurospheres are susceptible to HIV-1 infection and
414 that stem cell EVs may exert neuroprotective effects, we next assessed the potential functional effects of stem cell
415 EVs on damaged neurons *in vitro*. Here, we utilized two-dimensional cultures of neuronal cells; to induce neuronal
416 damage cells were exposed to EVs derived from U1 cART-treated cells ("damaging EVs"). Our rationale was based

417 on results from previous studies showing that EVs from HIV-1 infected cells contain viral by-products (e.g. TAR,
418 Tat, Nef, *env*) that can be transferred to recipient cells [104, 105, 106, 107]. Thus, we hypothesized that exposure of
419 neurons to these damaging EVs would be characterized by a loss in cellular viability and, moreover, that stem cell
420 EVs may have the potential to reverse this effect.

421 For this assay neurons were treated with EVs from either U1 cART-treated cells or a combination of U1
422 cART EVs with stem cell EVs. Representative images in Fig. 6c show that after approximately eight days in culture
423 the untreated cells appeared healthy, well-attached, and exhibited a spindle-like morphology. Conversely, neurons
424 exposed to U1 cART EVs displayed an altered appearance that was characterized by a reduction in attachment and
425 clumping/ aggregation of the remaining attached cells. However, treatment with either iPSC or MSC EVs at an
426 approximate ratio of 1:1000 (recipient cell: EV) promoted the re-attachment and spreading of cells that more closely
427 resembled the untreated control culture. To ascertain whether these effects may be mediated by EV-associated
428 RNA, stem cell EVs were exposed to UV(C) irradiation to deactivate RNA. Treatment of neurons with irradiated
429 EVs appeared to abrogate the morphological effects associated with non-irradiated stem cell EVs. Cellular viability
430 was next assessed using a luminescence-based assay. As shown in Fig. 6d, treatment of neurons with U1 cART EVs
431 resulted in a slight decrease in viability relative to the control. While the treatment with stem cell EVs did improve
432 cellular viability, only iPSC EVs were associated with a significant ($p < 0.05$) increase. Furthermore, there were no
433 significant effects of UV(C) irradiated EVs on cellular viability.

434 In a separate experiment, we have also utilized EVs isolated from cells infected with the human
435 coronavirus OC43 to induce neuronal damage (Supplementary Fig. 7). Similar to what was observed with U1 cART
436 EVs, neurons exposed to OC43 EVs detached from the substrate and appeared round in morphology. Again,
437 treatment with both iPSC and MSC EVs appeared to permit the re-attachment and spreading of cells. Exposure to
438 OC43 EVs also resulted in a strong reduction of neuronal viability and treatment with both iPSC and MSC EVs
439 significantly abrogated this effect ($p < 0.0001$). Moreover, exposure of stem cell EVs to UV(C) irradiation
440 substantially inhibited their ability to restore cellular viability. Collectively, these results suggest that stem cell EVs
441 have the potential to reverse the damaged phenotypes associated with infection and that EV-associated lncRNA may
442 be partially responsible for mediating this effect. Future studies will focus on optimizing these experiments to better
443 characterize the mechanism(s) associated with virally induced damage and stem cell EV-mediated repair.

444 **Discussion**

445 Throughout the last decade, iPSCs and their derivatives have revolutionized the fields of regenerative
446 medicine, drug development, and disease modeling [11]. With respect to the CNS, iPSC-derived NPCs and NSCs
447 have been used to successfully generate 3D neuronal cultures, or neurospheres. Relative to traditional 2D cultures,
448 3D models are expected to serve as a more relevant platform for the study of biological processes. For example,
449 neurospheres have the potential to provide enhanced molecular insight into key cellular processes relating to
450 migration, replication, apoptosis [27]. Additionally, their ability to be cultured in serum-free and chemically defined
451 conditions renders them particularly important for studies pertaining to neural development and neurogenesis [32].
452 Thereby, neurospheres may represent an ideal platform for preliminary *in vitro* studies surrounding the pathogenesis
453 of various neurological diseases and disorders. Previous works by others have utilized 3D neuronal cultures to
454 successfully model Zika and HSV-1 infections [33, 34, 35, 48]. To the best of our knowledge, this is the first study
455 utilizing NPC-derived neurospheres for retroviral infection.

456 The use of well-characterized and qualified material, as well as the establishment of robust and
457 reproducible protocols is essential for ensuring the integrity of scientific data. The protocols employed here
458 permitted the efficient formation of neurospheres, resulting in well-defined cultures that displayed uniformity in size
459 and appearance throughout the duration of the study; thereby overcoming some of the challenges that have
460 historically been associated with use of 3D neuronal cultures [51]. The NPCs used for these experiments also
461 underwent extensive characterization to authenticate not only their identity, but also their differentiation potential.
462 Our data suggests that NPC-derived neurospheres maintain their ability to differentiate into both mature neurons
463 (e.g. dopaminergic, GABAergic, glutamatergic) and glial cells (i.e. astrocytes and potentially microglia) in 3D
464 cultures. It is worth noting that properly distinguishing between microglia and macrophages has historically been
465 challenging as these cell types are often associated with many of the same surface markers. Due to the difficulties
466 associated with their phenotypic identification, here we use the term "microglia-like cells" to designate cells that
467 express either CD163 or CD11b, as these markers have previously been detected in either resting or activated
468 microglia and macrophages [108, 109, 110, 111, 112]. Another point worth highlighting is that the expression of
469 cell-specific markers may vary in response to different biological and biochemical parameters such as cell
470 maturation, cell culture conditions, and the inherent phenotypic heterogeneity within a given cell type [113]. Along
471 these lines, although we did not detect expression of the microglia marker Iba-1 in our neurospheres, D'Aiuto et al.

472 recently utilized human iPSC-derived NPCs to generate scaffold-free adherent 3D neuronal cultures which
473 expressed not only neuronal (glutamatergic, GABAergic, dopaminergic) markers but also GFAP and Iba-1 [35].
474 These authors also noted that 3D cultures were differentiated for a period of six weeks. When considering that the
475 neurospheres used for our experiments were cultured in the presence of differentiation medium for only a period of
476 two weeks, we suspect that extending this timeframe by several weeks could further improve the expression levels
477 of differentiated cells and allow for better characterization of cellular sub-populations. In addition, we suspect that
478 exposure of neurospheres to a stimulating agent (e.g. LPS) could further promote the expression of a microglial-like
479 phenotype.

480 Despite being regarded as "immune privileged," the CNS contains at least three types of immune cells,
481 namely CD4+ T cells, macrophages, and microglia, that can be infected by HIV-1 and subsequently serve as viral
482 reservoirs [58]. In the CNS, HIV-1 can activate numerous inflammatory mediators and enzymes that disrupt
483 downstream signaling pathways in both neuronal and glial cells [114]. HIV-1 infection is also associated with a
484 range of neurological symptoms collectively known as HAND, and the release of toxic viral proteins by infected
485 cells is expected to contribute to HAND pathogenesis [5,6,7,8]. However, the underlying mechanisms remain
486 poorly understood; consequently, there is a need to develop advanced assays to better characterize the molecular
487 mechanisms that contribute to HAND and other HIV-1 associated disease phenotypes. In these studies we sought to
488 assess the feasibility of using NPC-derived neurospheres for future studies modeling HIV-1 infection.

489 Dual-tropic HIV-1 89.6 utilizes the CXCR4 and CCR5 coreceptors; both of which are expressed on
490 resident CNS cells including macrophages, microglia, and astrocytes [114]. Whether or not astrocytes can harbor
491 productive infection remains a matter of debate; although integrated HIV-1 has been detected in astrocytes isolated
492 from infected patients and it has been reported that infected astrocytes can produce viral proteins (e.g. Tat, Rev, Nef)
493 that contribute to neuroinflammation and neuronal damage [2, 58, 61, 115, 116, 117, 118]. Results from our
494 experiments confirmed viral replication in neurospheres as evidenced by the expression of p24 capsid protein,
495 uncleaved Gag polyprotein Pr55, and accessory protein Nef, all of which were detected after seven days in culture.
496 As a measure of validation, we also detected p24 in neurospheres exposed to two other lab-adapted strains (JR-CSF
497 and CHO40). IP assays further revealed that the highest copies of HIV-1 TAR DNA were associated with
498 microglia-like cells. The JR-CSF infected sample also displayed relatively high copy numbers of TAR DNA
499 associated with astrocytes; a finding that is not entirely surprising given that this viral isolate originated from the

500 cerebrospinal fluid of an infected patient. Overall, this data is in agreement with HIV-1 tropism towards glial-like
501 cells. However, the current study does not directly address HIV-1 integration as only the total levels of TAR DNA
502 are reported. Thus, these transcripts may represent a mixture of both non-integrated DNA as well as integrated
503 proviral DNA. To quantify the level of HIV-1 integration in neurospheres, follow up studies employing an *Alu* PCR
504 assay can be performed to assess integration sites and levels of gene expression, as previously described [119, 120,
505 121, 122]. This information will provide more thorough insight into the efficiency of infection and the efficacy of
506 cART in 3D cultures.

507 Interestingly, we observed unique expression profiles of cell-specific markers among uninfected and
508 infected neurospheres (Fig. 3a). First, these results are in general agreement with our previous assays (ICC and IP)
509 which relied on the use of antibodies associated with astrocytes (GFAP), microglia-like cells (CD11b, CD163),
510 neurons (FOXA2, GAD65), and NSCs (SOX2) as varying levels of expression for each of these markers was
511 detected. GFAP is an intermediate filament protein that is most commonly associated with astrocytes and increased
512 GFAP expression is a hallmark of astrocyte activation (e.g. astrogliosis or astrocytosis) [123, 124]. Our observation
513 of increased GFAP expression in HIV-1 infected neurospheres is consistent with previous literature that has
514 characterized HIV-1 infection by astrocytosis [125, 126, 127]. As indicated previously, CD11b is an integrin
515 protein that can be used to identify either resting or activated microglia-like cells. Our observation of relatively
516 consistent CD11b expression may be related to the specificity of the antibody used. While the apparent increase in
517 the expression levels of neuronal markers ($TH^+$, $GAD65^+/67^+$, $BNPI^+$) in HIV-1 infected neurospheres were
518 unexpected, further studies are warranted to see if this phenotype reproduces. Without having an accurate
519 quantification of the cellular composition of neurospheres, it cannot be ruled out that some samples had inherently
520 higher levels of certain cell types to begin with. In addition, the spatial location of certain cell types within each
521 sphere needs to be considered. For example, it may be possible that more mature cell types are located towards the
522 center of the sphere while cells around the periphery may represent a population of progenitor/proliferating cells.
523 Without knowing the kinetics of HIV-1 infection in this 3D platform, it is also possible that the virus was not able to
524 efficiently penetrate the neurospheres; along these lines, an incubation period longer than seven days may be
525 required to better assess the long-term effects of HIV-1 infection on certain cell types. Nonetheless, we believe that
526 these novel results provide a justifiable proof-of-concept for continued studies that can further fine tune these
527 experimental details.

528 The primary focus of this manuscript surrounds retroviral infections, namely HIV-1 and HTLV-1. HTLV-
529 1 is the etiological agent of both adult T cell leukemia (ATL) and the progressive neurological disorder known as
530 HTLV-1-associated myelopathy/tropical spastic paraparesis (HAM/TSP) [62, 63, 64, 65]. As in the case of HIV-1,
531 the underlying mechanisms contributing to HTLV-1 associated pathologies remain poorly understood. Thus, there
532 is an imminent need for the identification of suitable *in vitro* platforms to drive the field of HTLV-1 research.
533 Exposure to IR is known to initiate cell cycle arrest; moreover, we have recently published data using IR to activate
534 transcription of HTLV-1 in HUT 102 cells [66, 67, 68, 128]. Therefore, we rationalized that co-culturing of
535 irradiated HUT 102 cells with neurospheres would provide a reliable platform to assay for infection. To this end, we
536 performed western blot to assess the relative expression of Tax and p19, two indicators of HTLV-1 viral replication.
537 When accounting for background levels in the non-irradiated HUT 102 control sample, there were clear increases in
538 the expression of both Tax and p19. RT-qPCR also confirmed increased gene expression of *tax, env*, and to a much
539 lesser extent, *hbz*, in the co-cultures. Treatment with IFN/AZT was also associated with reductions in the
540 corresponding protein/gene expression levels. Therefore, this preliminary data suggests that neurospheres may be
541 reliable models for studying the mechanisms surrounding HTLV-1 associated neuropathogenesis. Future
542 experiments will utilize other HTLV-1 and HIV-1 infected cells (e.g. U1) that have been irradiated to potentially
543 increase viral spread.
544 In recent years our laboratory has also focused extensively on EVs and considerable efforts have been
545 made in the characterization of EVs from both infected and non-infected cells [68, 72, 105, 106, 107, 129, 130, 131].
546 Here specifically, we were interested in examining the functional effects of stem cell EVs on HIV-1 infected
547 neurospheres. Our rationale was based on the results from numerous studies which have highlighted the protective
548 and reparative properties of stem cell EVs among various CNS pathologies, as reviewed elsewhere [42, 46, 47, 132].
549 For these studies we utilized well-characterized preparations of iPSC and MSC EVs that have previously
550 demonstrated reparative effects in various *in vitro* assays (e.g. cellular migration, cellular viability, angiogenesis)
551 [72].
552 The results from our uptake assays first confirmed that EVs were capable of penetrating neurospheres.
553 Moreover, fluorescently labeled EVs remained detectable for at least eight days post-treatment. These results were
554 consistent among two independent experiments that used different fluorescent probes to stain either EV lipid
555 membranes or EV-associated RNA. Interestingly, gelatin zymography indicated that iPSC and A549 EVs had

556 relatively high levels of the active forms of the gelatinases MMP9 and MMP2 as compared to MSC EVs. While we
557 observed distinct differences in the morphological appearance of iPSC EV and A549 EV-treated neurospheres, it is
558 imprudent to attribute this effect to any specific EV cargo at this time. More importantly, these results demonstrated
559 feasibility and provided the justification for subsequent experiments focused on the functional effects of stem cell
560 EVs in neurosphere cultures.

561 As previously mentioned, over amplification of inflammatory pathways, coupled with the release of toxic
562 viral proteins from infected cells, is believed to contribute to the neuronal damage associated with HIV-1 [5,6,7,8].
563 Additionally, activated microglia release neurotoxic factors including cytokines and chemokines (e.g. IL6, IL8,
564 IL1β, TNFα, IFNα) that can further exacerbate the inflammatory response [60, 114]. In recent years, the
565 neuroprotective and anti-inflammatory properties of stem cell EVs have been well-documented; in the context of the
566 CNS, there is accumulating evidence that stem cell EVs may be able to reverse neuronal apoptosis and modulate the
567 polarization of both astrocytes and microglia from pro-inflammatory to anti-inflammatory phenotypes [81, 82, 83,
568 84, 85, 86, 87, 88, 89, 90, 91, 92]. To the best of our knowledge, the functional effects of stem cell EVs on 3D
569 cultures has not previously been reported.

570 As expected, we observed increased expression of pro-inflammatory cytokines TNFα, IL-8, and IL-1β in
571 HIV-1 infected neurospheres. Additionally, we also observed increased expression of both cleaved PARP-1 and p-
572 p53 (ser-15) in response to HIV-1 infection. These findings are consistent with the activation of cellular stress
573 response pathways as cleavage of PARP is commonly regarded as a hallmark of apoptosis [133, 134] and serine 15
574 phosphorylation is associated with p53 activation and the subsequent initiation of cell cycle checkpoints and DNA
575 repair mechanisms [135, 136, 137]. The addition of stem cell EVs to HIV-1 cART-treated neurospheres abrogated
576 each of these effects; thereby pointing towards a potential EV-mediated reversal of inflammatory and apoptotic
577 signaling. There were no apparent increases in the expression of cleaved caspase-3 among any samples. Since
578 caspase-3 is classically regarded as an "executioner" caspase [138, 139] this data suggests that damaged cells may
579 have been in the early stages of apoptosis, thus making them more receptive to reparative intervention. Future
580 experiments will focus on examining the expression levels of p53 kinases (e.g. ATM, ATR), as well as the
581 expression of different apoptotic regulators (e.g. Bcl-2, Bax, Bid), to better define the reparative mechanisms of
582 stem cell EVs.

583 EVs are associated with a rich diversity of cargo which includes various non-coding RNAs (i.e. small non-

584 coding and long non-coding RNAs), as described elsewhere [140, 141, 142, 143, 144, 145]. Mechanistically
585 speaking, this cargo is expected to drive the functional effects that are attributed to EVs. Although many studies
586 have evaluated the reparative potential of various EV-associated miRNAs, the characterization of EV-associated
587 lncRNAs remains largely unexplored. While the data from our lncRNA analysis highlighted distinct differences
588 among A549 (cancer) EVs and stem cell EVs, particularly with respect to chromosome localization and patterns of
589 differentially expressed transcripts, a more comprehensive assessment of this data is outside of the scope of the
590 current manuscript. However, the identification of at least two iPSC EV-associated lncRNAs (i.e. AC120498.9,
591 ADIRF-AS1) whose secondary structures contained sequences of double-stranded RNA ≥ 30 bp in length led us to
592 examine their interactions with different RNA binding proteins *in vitro*, as this property has previously been linked
593 to the activation of PKR [102, 103]. Indeed, we found that the relevant sequences of these lncRNAs were capable of
594 binding not only to PKR, but also to other dsRNA binding proteins, namely DICER, RIG-I, and ADAR1 in neurons,
595 astrocytes, and MDMs. Although we are unable to conclude the significance of this binding at the present time, we
596 speculate that it may represent a novel form of RNA interference by which certain EV-associated lncRNAs bind to
597 host RNA binding proteins, including innate immune molecules, to alter their function. This area of research
598 requires further attention to better characterize the downstream functional effects of this binding. Lastly, when
599 mapping the secondary structures of iPSC EV-associated lncRNAs, we also noticed that many of these structures
600 each contained multiple circular loops that resemble the structure of circular RNAs (circRNAs). For reference,
601 these structures are shown in Supplementary Fig. 8. While circRNAs represent a relatively novel class of non-
602 coding RNAs, there is emerging evidence to suggest that they may predominantly function as miRNA sponges to
603 prevent binding of miRNAs to their target genes [146, 147]. Future experiments will explore this possibility in the
604 context of stem cell EV-mediated repair.

605 It has been shown that EVs released from HIV-1 infected cells contain viral by products including Nef, Tat
606 *env*, and TAR [104, 105, 107, 148]. The effects of these damaging EVs include rendering recipient cells more
607 susceptible to infection, enhancing the spread of infection, and induction of cellular death, as recently reviewed
608 [149]. Since we were unable to directly study their effects in HIV-1 infected neurospheres, we utilized 2D cultures
609 of neurons to determine if exposure to EVs from HIV-1 infected cells could induce neuronal death and,
610 subsequently, to assess whether stem cell EVs could exert any functional effects on damaged cells. Our data
611 confirmed a decline in cell healthy and slight reduction in viability upon treatment with damaging EVs, while stem

612 cell EVs appeared to reverse these processes. Even though UV(C) treatment did not have a significant impact on
613 cellular viability, the observed morphological differences in neurons treated with irradiated stem cell EVs relative to
614 non-irradiated EVs suggests that UV(C) may have partially impaired the functional effects of both iPSC and MSC
615 EVs. On the other hand, performance of the same assay using OC43 EVs to induce neuronal damage produced
616 considerable outcomes. Here, treatment of damaged cells with stem cell EVs yielded a significant increase in
617 viability whereas UV(C) irradiation abrogated their effects. Thus, these experiments highlight the existence of
618 different mechanisms surrounding both EV-induced damage and EV-mediated repair in recipient cells.
619 Overall, the results from this study have demonstrated that NPC-derived neurospheres are susceptible to
620 retroviral infection and, therefore, may serve as an alternative platform for studying the molecular mechanisms
621 associated with HIV-1. Moreover, we also demonstrated the functional relevance of stem cell EVs in the context of
622 mediating cellular repair induced by viral damage. Importantly, this data is in consensus with numerous other
623 studies which have described the neuroprotective and anti-inflammatory properties of stem cell EVs. We
624 acknowledge that further experiments are necessary to more carefully define and characterize the mechanisms
625 contributing to both viral-induced damage and EV-mediated repair. However, based upon the current data, we
626 hypothesize that the functional effects of stem cell EVs in both uninfected and virally infected cells may be partially
627 mediated through the interactions between EV-associated lncRNAs and nucleic acid sensors (e.g. PKR, ADAR1,
628 RIG-I) in recipient cells. For example, in uninfected cells this binding could trigger the activation of intracellular
629 signal transduction pathways, thereby resulting in increased production of interferon and a potent antiviral response
630 that may ultimately protect the cell from viral infection. Conversely, infected cells would have already mounted an
631 immune response to undergo cell cycle arrest. In this scenario, EV-associated lncRNAs could prolong this effect by
632 binding to, and thus inactivating, the host innate immune molecules to prevent further viral replication. In turn, this
633 would also dampen the production of damaging EVs from infected cells. Over time, the EV-associated cytokines
634 and growth factors will promote cellular replication of both infected and uninfected cells. However, we believe that
635 the net outcome will confer an overall protective effect, since we suspect that uninfected cells represent a majority
636 (≥ 90%) of the total cell population. In support of this, we have data showing that treatment of HIV-1 infected
637 neurospheres with stem cell EVs results in increased expression of different cell populations including NPCs,
638 astrocytes, and microglia-like cells (data not shown). Thus, we believe that this research sets an important precedent

639 for the continued use of NPC-derived neurospheres for modeling biological processes relating to the CNS. We look
640 forward to utilizing these cultures to further expand our knowledge in this area.

641
642
643
644
645
646
647
648
649
650
651
652
653
654
655
656
657
658
659
660
661
662
663
664
665
666
667
668
669

670 **Methods**

671 **Cell Culture**

672 **NPCs and Neurospheres**

673 Normal Human Neural Progenitor Cells (ATCC® ACS-5003™) were expanded per the manufacturer's
674 recommendations. Cells were cultured with STEMdiff™ Neural Progenitor Medium (STEMCELL technologies™)
675 in cell matrix-coated flasks. Media was changed every other day. Cells were subcultured using Accutase diluted
676 1:1 with PBS. To generate neurospheres, NPCs were seeded at approximately 1.0 x $10^5$ cells per well in ultra-low
677 attachment, U-shaped bottom 96-well plates in Neural Progenitor Medium. After approximately 48 hours, the
678 medium was removed from the wells and replaced with DMEM:F12 (ATCC® 30-2006™) + Dopaminergic Neuron
679 Differentiation Kit (ATCC® ACS-3004™) to induce differentiation. Neurospheres received a media replacement
680 every 2 to 3 days for a period of 2 weeks. Phase contrast images were acquired using an inverted microscope and
681 calibrated measurements were performed using Zen imaging software (Zeiss).

682 **Cell Lines**

683 The human neuroblastoma cell line SHSY5Y (CRL-2266™), the human astrocytoma cell line CCF-STTG1
684 (CRL-1718™), human monocytic leukemia cell line THP-1 (TIB-202™), and the human lung carcinoma cell line
685 A549 (CCL-185™) were obtained from the American Type Culture Collection (ATCC). SHSY5Y cells were
686 cultured in a 1:1 mixture of EMEM (ATCC® 30–2003™) and F-12K (ATCC® 30–2004™) supplemented with
687 10% fetal bovine serum (FBS) (ATCC® 30–2020™). CCF-STTG1 and THP-1 cells were cultured in RPMI-1640
688 (ATCC® 30–2001™) supplemented with 10% FBS. A549 cells were cultured in F-12K (ATCC® 30–2004™)
689 supplemented with 10% FBS. Cells were maintained in culture following the manufacturer's recommendations.
690 HIV-1 infected U937 Cells (U1; NIH AIDS Reagent Program) were cultured in RPMI-1640 supplemented with 10%
691 exosome-depleted FBS.

692 To generate MDMs, THP-1 cells and U1 cells were treated with phorbol 12-myristate 13-acetate (PMA;
693 100 nM) and incubated for 4 to 5 days. U1-MDMs then received 2 treatments of cART (emtricitabine, tenofovir
694 disoproxil fumarate, ritonavir, darunavir; 2.5 μM each) over a 5 day incubation period.

695 **Immunocytochemistry (ICC)**

696 Cells were fixed in 4% paraformaldehyde. ICC was performed following standard protocols. After

697 permeabilization (0.2% Triton X-100+ 0.01% Tween® 20) and blocking (5% goat serum), cells were incubated
698 overnight with the following primary antibodies: α-FOXA2 (Santa Cruz Biotechnology sc-101060), α-GFAP (Santa
699 Cruz Biotechnology sc-166481), α-CD163 (Santa Cruz Biotechnology sc-20066), α-Iba-1 (Santa Cruz
700 Biotechnology sc-32725), α-Tubulin β 3 (Tuj1; Biolegend MMS-435P), α- Tyrosine Hydroxylase (TH; Millipore
701 AB152). The appropriate secondary antibody (Alexa Fluor 488 goat anti-rabbit or Alexa Fluor 594 goat anti-rabbit)
702 was then added for 1 hour. Nuclei were counter-stained with DAPI and fluorescent imaging was performed using a
703 Zeiss Axio Observer.Z1 microscope fitted with the appropriate filters.

704 **Infection of Neurospheres**

705 **HIV-1 Infection**

706 Differentiated neurospheres were infected with either dual-tropic HIV-1 89.6 (MOI:10; ~250 ng of p24),
707 JR-CSF (MOI:10), or CHO40 (MOI:10) and InfectinTM (Virongy, LLC). The total final volume of spheres + virus
708 + Infectin was approximately 200 µL. After 48 hours of incubation (day 2), neurospheres were gently washed with
709 PBS and received fresh differentiation media with or without cART cocktail (lamivudine (NRTI), tenofovir
710 disoproxil fumarate (NRTI), emtricitabine (NRTI), indinavir (protease inhibitor); 2.5 µM each). HIV-1 89.6 +
711 cART neurospheres also received treatment with stem cell EVs at an approximate ratio of 1:250 (uninfected
712 recipient cell to EV). Neurospheres received additional cART and EV treatments on day 5. After 7 days the
713 neurospheres were harvested for downstream analysis.

714 **HTLV-1 co-culture**

715 HUT 102 cells (log phase) were cultured in RPMI-1640 supplemented with 10% heat-inactivated,
716 exosome-depleted FBS for 5 days. Cells were then seeded at 1.0 x $10^6$ viable cells/mL and exposed to IR using a
717 RS-2000 X-Ray Irradiator (Rad Source Technologies) at a dose of 10 Gy. Irradiated cells were co-cultured with
718 differentiated neurospheres (day 0) at an approximate ratio of 1:100 (infected cells: uninfected cells in neurospheres)
719 with or without combination treatment of interferon-α (10 K unit) and zidovudine (20 µM), hereafter referred to as
720 IFN/AZT. Treatments were added on days 3 and 5. After 7 days the neurosphere co-cultures were harvested for
721 downstream analysis.

722 **Western Blot**

723 Protein lysates from neurospheres were analyzed via Bradford assay following the manufacturer's

724 recommendations (Bio-Rad). For western blot, equal amounts of protein were mixed with Laemmli buffer, heated at
725 95°C, and separated on a 4-20% Tris-glycine SDS gel (Invitrogen). Proteins were transferred to an Immobilon
726 PVDF membrane (Millipore) overnight at 50 milliamps. After blocking the membrane with 5% milk in PBS with
727 0.1% Tween®-20, the appropriate primary antibody was added for overnight incubation at 4 °C. Antibodies used
728 for these experiments included α-p24 (NIH AIDS Reagent Program), α-Nef (NIH AIDS Reagent Program), α-Tax
729 (kindly provided by Dr. Scott Gitlin, University of Michigan), α-p19 (Santa Cruz Biotechnology sc-1665), α-
730 Integrin αM (Santa Cruz Biotechnology sc-515923), α-CD163 (Santa Cruz Biotechnology sc-20066), α- glutamine
731 synthetase (Santa Cruz Biotechnology sc-74430), α-GFAP (Santa Cruz Biotechnology sc-166481), α-Tyrosine
732 Hydroxylase (Millipore Sigma AB152), α-FOXA2 (Santa Cruz Biotechnology sc-101060), α-GAD-65 (Santa Cruz
733 Biotechnology sc-377145), α-GAD-67 (Santa Cruz Biotechnology sc-28376), α-BNPI (Santa Cruz Biotechnology
734 sc-377425), α-SOX2 (Santa Cruz Biotechnology sc-365823), α-PARP-1 (Santa Cruz Biotechnology sc-7150), α-p-
735 53 (Cell Signaling Technology 2524S), α-p-53 (ser-15) (Cell Signaling Technology 9286S), α-p-p21 (ser-146)
736 (Santa Cruz Biotechnology sc-12902), α-Caspase 3 (Santa Cruz Biotechnology sc-7148), α-TNFα (Santa Cruz
737 Biotechnology sc-52749), α-IL-8 (Santa Cruz Biotechnology sc-376750), α-IL-1β (Santa Cruz Biotechnology sc-
738 32294) , α-PKR (Santa Cruz Biotechnology sc-136352), α-DICER (Cell Signaling Technology 3363S), α-ADAR1
739 (Santa Cruz Biotechnology sc-271854) , α-RIG-I (Santa Cruz Biotechnology sc-376845), α-MMP9 (Cell Signaling
740 Technology 2270S), and α-Actin (Abcam ab-49900). Membranes were subsequently washed, incubated with the
741 appropriate secondary antibody at 4 °C, and then immediately developed using either Clarity™ or Clarity Max™
742 Western ECL Substrate (Bio-Rad). Chemiluminescence imaging was performed with the ChemiDoc™ Touch
743 Imaging System (Bio-Rad).

744 **Reverse Transcription and Quantitative PCR**

745 Total RNA from neurosphere cultures was extracted using TRIzol™ reagent (Invitrogen) following the
746 manufacturer's recommendations. Reverse transcription was carried out with the GoScript™ Reverse Transcription
747 System (Promega) following the manufacturer's recommended protocols. The following specific primers were
748 used: HIV-1 trans-activation response (TAR) reverse primer (5′-CAA CAG ACG GGC ACA CAC TAC-3′,
749 Tm = 58 °C), HIV-1 envelope reverse primer: (5′-TGG GAT AAG GGT CTG AAA CG-3′, Tm = 58 °C), HTLV-1
750 Tax reverse primer (5′- AAC ACG TAG ACT GGG TAT CC-3′, Tm = 53.6°C), HTLV-1 bZIP factor (HBZ) reverse
751 primer (5′-TGA CAC AGG CAA GCA TCG-3′, Tm = 55.7°C), HTLV-1 envelope reverse primer (5′-CCA TCG

752 TTA GCG CTT CCA GCC CC-3′, Tm = 64.4°C) [68, 129].

753 qPCR for HIV-1 TAR and envelope was carried out with IQ Supermix (Bio-Rad). The following
754 primers/probes were used: TAR forward primer (5′-GGT CTC TCT GGT TAG ACC AGA TCT G-3′, Tm = 60 °C),
755 TAR reverse primer (5′-CAA CAG ACG GGC ACA CAC TAC-3′, Tm = 58 °C), TAR Probe ( 5'-56-FAM-AGC
756 CTC AAT AAA GCT TGC CTT GAG TGC TTC-36-TAMSp-3', Tm = 63.2°C). Serially diluted DNA from HIV-1
757 8E5 cells (NIH AIDS Reagent Program) were included as standards [129]. The reaction conditions were 50°C for 2
758 minutes (1 cycle), 95 °C for 3 minutes (1 cycle), 95 °C for 15 seconds and 60°C for 40 seconds (41 cycles).
759 Quantification was determined from the average cycle threshold (Ct) values of each sample relative to the standard
760 curve. All reactions were run triplicate on the CFX96™ Real-Time PCR Detection System (Bio-Rad).

761 qPCR of HTLV-1 Tax, HBZ, and envelope was carried out with SYBR® Green Master Mix (Bio-Rad)
762 using the following primers: Tax forward primer (5′- ATC CCG TGG AGA CTC CTC AA-3′, Tm = 57.6°C), Tax
763 reverse primer (5′- AAC ACG TAG ACT GGG TAT CC-3′, Tm = 53.6°C), HBZ forward primer (5′-AGA ACG
764 CGA CTC AAC CGG-3′, Tm = 57.8°C), HBZ reverse primer (5′-TGA CAC AGG CAA GCA TCG-3′, Tm =
765 55.7°C), envelope forward primer (5′-CGG GAT CCT AGC GTG GGA ACA GGT-3′, Tm = 64.5°C), envelope
766 reverse primer (5′-CCA TCG TTA GCG CTT CCA GCC CC-3′, Tm = 64.4°C). Serially diluted DNA from HTLV-
767 1 infected cells (HUT 102) served as standards [68]. The reaction conditions were as follows: Tax: 50°C for 2
768 minutes (1 cycle), 95°C for 2 minutes (1 cycle), 95°C for 15 seconds, 51°C for 20 seconds, and 72°C for 40 seconds
769 (40 cycles), 65°C for 5 seconds (1 cycle), 95°C for 5 seconds (1 cycle); HBZ: 50°C for 2 minutes (1 cycle), 95°C for
770 2 minutes (1 cycle), 95°C for 15 seconds, 65.7°C for 20 seconds, and 72°C for 40 seconds (40 cycles), 65°C for 5
771 seconds (1 cycle) and 95°C for 5 seconds (1 cycle); envelope: 50°C for 2 minutes (1 cycle), 95°C for 2.5 minutes (1
772 cycle), 95°C for 15 seconds and 64°C for 40 seconds (40 cycles), 65°C for 5 seconds (1 cycle), and 95°C for 5
773 seconds (1 cycle) [68]. Sample quantification was determined from the average cycle threshold (Ct) values of each
774 sample relative to the standard curve. All reactions were run in triplicate on the CFX96™ Real-Time PCR
775 Detection System (Bio-Rad).

776 **Isolation and Characterization of EVs**

777 **Stem Cell EVs and A549 EVs**

778 EV isolation was performed as previously described [72]. Briefly, human bone marrow MSCs (BM-

779 MSCs) (ATCC® PCS-500-012™) and human lung carcinoma cell line A549 (ATCC® CCL-185™) were cultured
780 in the presence of exosome-depleted FBS (Thermo Fisher Scientific) prior to collection of conditioned medium.
781 Human iPSCs (ATCC® ACS-1019™), which were cultured in serum-free/xeno-free medium, received full media
782 changes every day and the conditioned medium was collected and stored at 4°C throughout expansion. Bulk
783 conditioned medium was first spun at 2,000 x g and then filtered with a 0.22 µm filter to remove cellular debris and
784 larger vesicles. Filtered medium then underwent concentration and buffer exchange via tangential flow filtration
785 (TFF) (Spectrum®) to isolate EVs. Samples were subsequently aliquoted and frozen at -20°C for downstream
786 analysis. The size distribution and concentration of each EV sample was assessed via nanoparticle tracking analysis
787 (NTA) using the NanoSight®NS300 (Malvern Panalytical). Prior to analysis the equipment was calibrated per the
788 manufacturer's protocols. EV samples were diluted in sterile PBS immediately before measurement. The acquired
789 data was analyzed by the instrument's built-in software.

790 **HIV-1 and Human Coronavirus OC43 EVs**

791 U1 cART EVs were isolated via ultracentrifugation. First, supernatants were centrifuged at 1,200 rpm for 5
792 minutes to pellet any cellular debris. The resulting supernatant was then centrifuged at 100,000 x g for 90 minutes
793 using the 70Ti rotor (Beckman). The pellet was washed with PBS followed by another centrifugation at 100,000 × g
794 for 90 minutes. EV pellets were resuspended in PBS and then frozen at -20°C for downstream analysis.
795 A549 cells were infected with 5.0 x $10^5$ TCID50 of human coronavirus OC43 for 96 hours. Supernatants
796 were collected and centrifuged at 2,000 rpm for 5 minutes, filtered through a 0.22 µm sterile filter, and then
797 centrifuged at 100,000 x g for 90 minutes using the 70Ti rotor (Beckman). The pellet was resuspended in sterile
798 PBS and treated with 45 mJ/$cm^3$ of UV(C) LED irradiation. Samples of UV(C)-treated EVs (1, 5, 10 uL) were
799 added to Vero cells for two passages and no viral outgrowth was detected (data not shown). Remaining EVs were
800 frozen at -20°C for downstream analysis.
801 U1 cART and OC43 EVs were analyzed via NTA using the ZetaView® Z-NTA (Particle Metrix). Prior to
802 analysis the equipment was calibrated per the manufacturer's recommendation and each EV sample was diluted in
803 deionized water prior to analysis. The acquired data was analyzed by the instrument's built-in software.

804 **EV Uptake**

805 EVs were labeled with either SYTO® RNASelect Green Fluorescent Stain (Thermo Fisher) or BODIPY™

806 493/503 (Thermo Fisher) following the manufacturer's recommended protocol. Excess dye was removed via
807 centrifugation using a Sephadex® G-10 (Sigma-Aldrich) column with a glass wool bottom packed with 0.75 mL
808 beads. Labeled EVs were added to differentiated neurospheres and incubated at 37°C. Fluorescent imaging was
809 performed using a Zeiss Axio Observer.Z1 microscope fitted with the appropriate filter.

810 **RNA Sequencing and Analysis**

811 Total RNA was extracted from EVs using TRIzol™ reagent (Invitrogen) following the manufacturer's
812 recommendations. RNA sequencing and sequence analysis was performed by LC Sciences, LLC. Briefly, the 2100
813 Bioanalyzer System (Agilent) was used to analyze total RNA and ribosomal RNA was removed per the Ribo-Zero
814 Gold Kit (Illumina). The remaining RNA fragments were used to construct a strand-specific cDNA library using the
815 dUTP method (average library insert size was 300 ± 50 bp) and pair-end sequencing was performed using the Hiseq
816 4000 (Illumina) following the manufacturer's recommended protocol. Reads containing adaptor contamination and
817 low quality bases were removed with Cutadapt and in-house perl scripts [150]. FastQC was used to verify transcript
818 quality, Tophat2 [151] and Bowtie 2 [152] were used for mapping reads to the genome, and in-house Perl scripts
819 were used for GO and KEGG enrichment analysis. StringTie [153] was used for transcript assembly and Ballgown
820 [154] was used to perform differential expression analysis. Significant terms for GO analysis were determined by a
821 hypergeometric equation and GO terms with a p value <0.05 were considered significant.

822 The secondary structures of selected long non-coding RNAs were predicted using the RNAfold Server of
823 the ViennaRNA Websuite [155]. RNA sequences were first retrieved from NCBI and the FASTA sequence was
824 submitted to the server. This server predicted the minimum free energy (mfe) secondary structure of single
825 sequences using a programming algorithm originally developed by Zuker and Stiegler [156]. The secondary
826 structures were predicted using a temperature setting of 37 °C and keeping all other parameters to default [157].

827 **Immunoprecipitation for direct PCR**

828 Neurospheres were washed with PBS and treated with 0.25% Trypsin/EDTA (diluted 1:1 with PBS) for 3
829 to 5 minutes at 37°C. Trypsin was neutralized by the addition of RPMI-1640 with 10% FBS. The appropriate
830 antibodies (α-Integrin αM (Santa Cruz Biotechnology sc-515923); α-GFAP (Santa Cruz Biotechnology sc-166481),
831 α-GAD-65 (Santa Cruz Biotechnology sc-377145), α-SOX2 (Santa Cruz Biotechnology sc-365823)) were added (5
832 µg per 10E5 cells) and incubated at 4°C for 4 hours on a rotator. Protein A+G washed beads (30 µL; 30% slurry in

833 PBS with 0.01% BSA) were added to the cell/antibody mixture and incubated for 1.5 hours at 4°C. Samples were
834 spun at 1,000g for 5 minutes, washed once with PBS/BSA buffer, and pellets (protein A/G beads + cells + antibody
835 in ~25µl packed beads) were resupended in PBS (20 µL). Approximately 1/5 of the solution was used for direct
836 PCR. The first cycle of PCR (heat for strand separation) is sufficient to crack open viruses and eukaryotic cells. An
837 initial titration of an astrocyte cell line with antibody and beads was used to titrate the amount of beads/cell/antibody
838 needed for direct PCR using GAPDH primers (data not shown).

839 **RNA Pull-down**

840 The following RNA sequences were synthesized with 5' Biotin conjugates: UAGCUGGGAUUACAG
841 GCGUGCACCACCACACCCGGCUAAUUUUUGUAUUUUU (AC120498.9) and CUCACUGCAACCUCU
842 GCCUUCCAGGUUCAA (ADIRF-AS1). Whole cell lysate (SHSY5Y, CCF-STTG-1, or MDM) (approximately 75
843 µg) was incubated with approximately 10 µg of each biotinylated RNA overnight at 4°C. The next day,
844 Streptavidin-Sepharose beads (BioVision) were added and again incubated at 4°C for an additional 2 hours. The
845 samples were spun at 14000 x g and resuspended in TNE50 + 0.1% NP40. Samples were mixed with Laemmli
846 buffer for subsequent SDS/PAGE and western blot was performed for PKR, DICER, ADAR1, and RIG-I (as
847 described above).

848 **Cell Viability Assay**

849 SHYSY5Y cells were seeded in a 96-well plate (day 0). On day 1, cells were treated with either U1 cART
850 EVs (1:50,000 approximate cell to EV ratio) or OC43 EVs (1:6,500 approximate cell to EV ratio) to induce damage.
851 Stem cell EVs were treated with 45 mJ/cm3 of UV(C) LED irradiation to inactivate EV-associated RNA. Stem cell
852 EVs were subsequently added at an approximate ratio of 1:1000 (recipient cell to EV ratio). Untreated cells
853 received PBS. Each sample was performed in triplicate. Cells were observed daily. On day 8 representative
854 photographs were taken using an EVOS XL microscope and viability was assayed using the CellTiter-Glo®
855 Luminescent Cell Viability kit (Promega) per the manufacturer's protocol. Luminescence was measured with the
856 GloMax®-Multi Detection System (Promega).

857 **Zymography**

858 EVs were added to a 30% slurry of NT80/82 Nanotrap® particles (Ceres Biosciences) and PBS was added
859 to bring the final volume to 500 µL. Samples were rotated at 4°C for two hours, spun, and washed with PBS.

860 Laemmli buffer was added to each sample, heated for 10 minutes at 37°C, and then spun to pellet the Nanotraps.
861 The resulting supernatants were loaded on a Novex™ 10% Zymogram Plus (Gelatin) Protein Gel (ThermoFisher
862 Scientific). The gel was run at 120V for approximately 90 minutes, renatured for 30 minutes at room temperature
863 on a rocker, and incubated at 37°C in developing buffer for a period of 24 to 36 hours. After development, the gel
864 was gently stained for an additional 24 to 48 hours with Coomassie blue R-250. Imaging was performed with the
865 ChemiDoc™ Touch Imaging System (Bio-Rad).

866 **Statistical Analysis**

867 Analysis of quantitative data was performed by using Graph Pad Prism. The *P* values were determined via
868 analysis of variance (ANOVA) using multiple comparisons. To justify the use of ANOVA, experimental data was
869 assumed to approximate a normal distribution. *P* values were defined as follows: of greatest statistical significance
870 (< 0.0001), of greater significance (< 0.005), and significant (< 0.05).

871
872
873
874
875
876
877
878
879
880
881
882
883
884
885
886
887
888
889

**Acknowledgements**

We would like to thank all members of the Kashanchi lab for their contributions, especially Gwen Cox and interns Gabrielle Heller and Sahan Raghavan. We also would like express thanks to ATCC management, especially Drs. Mindy Goldsborough and James Kramer for supporting this work. This work was further supported by National Institutes of Health (NIH) Grants (AI078859, AI074410, AI127351-01, AI043894, and NS099029 to FK) and (R33 CA206937 and R01AR068436 to LAL). The content is solely the responsibility of the authors and does not necessarily represent the official views of the National Institutes of Health.

**Author Contributions**

H.B. wrote and edited the manuscript. D.Y. and S.J. contributed to development, characterization, and production of iPSCs and NPCs. H.B. and D.Y. contributed to the production of EVs. H.B., M.C., Y.K., P.K., J.E. carried out experiments and contributed to data analysis. L.A.L. and N.E. contributed to the experimental designs. F.K. contributed to the overall direction and coordination of the study as well as contributions to experimental design and data analysis.

**Competing Interests**

H.B., D.Y., and S.J. are employed by ATCC and L.A.L. is affiliated with Ceres Nanosciences, Inc. All other authors declare no potential conflicts of interest.

917 **References**


918 1. UNAIDS. Global HIV & AIDS statistics — 2019 fact sheet. PDF at
919 https://www.unaids.org/sites/default/files/media_asset/UNAIDS_FactSheet_en.pdf.

920 2. Saylor, D, *et al*. HIV-associated Neurocognitive Disorder--Pathogenesis and Prospects for Treatment. *Nat Rev*
921 *Neurol*. **12**, 234-48 (2016).

922 3. Chen, M.F., Gill, A.J., Kolson, D.L. Neuropathogenesis of HIV-associated Neurocognitive Disorders: Roles for
923 Immune Activation, HIV Blipping and Viral Tropism. *Curr Opin HIV AIDS*. **9**, 559-64 (2014).

924 4. Eggers, C, *et al*. HIV-1-associated Neurocognitive Disorder: Epidemiology, Pathogenesis, Diagnosis, and
925 Treatment. *J Neurol*. **264**, 1715-1727 (2017).

926 5. Ferrell, D. & Giunta, B. The Impact of HIV-1 on Neurogenesis: Implications for HAND. *Cell Mol Life Sci*. **71**,
927 4387-92 (2014).

928 6. Rao, V.R., Ruiz, A.P., Prasad, V.R. Viral and Cellular Factors Underlying Neuropathogenesis in HIV Associated
929 Neurocognitive Disorders (HAND). *AIDS Res Ther*. **19**;11:13 (2014).

930 7. Ru, W. & Tang, S.J. HIV-associated Synaptic Degeneration. *Mol Brain*. **10**, 40 (2017).

931 8. Teodorof-Diedrich, C. & Spector, S.A. Human Immunodeficiency Virus Type 1 gp120 and Tat Induce
932 Mitochondrial Fragmentation and Incomplete Mitophagy in Human Neurons. *J Virol*. **92**, e00993-18 (2018).

933 9. Kaushik, A., Jayant, R.D., Bhardwaj, V., Nair, M. Personalized Nanomedicine for CNS Diseases. *Drug Discov*
934 *Today*. **23**, 1007-1015 (2018).

935 10. GBD 2016 Neurology Collaborators. Global, Regional, and National Burden of Neurological Disorders, 1990-
936 2016: A Systematic Analysis for the Global Burden of Disease Study 2016. *Lancet Neurol*. **18**, 459-480 (2019).

937 11. Shi, Y., Inoue, H., Wu, J.C., Yamanaka, S. Induced Pluripotent Stem Cell Technology: A Decade of Progress.
938 *Nat Rev Drug Discov*. **16**, 115-130 (2017).

939 12. Takahashi, K. & Yamanaka, S. Induction of Pluripotent Stem Cells From Mouse Embryonic and Adult
940 Fibroblast Cultures by Defined Factors. *Cell*. **126**, 663-76 (2006).

941 13. Takahashi, K, *et al*. Induction of Pluripotent Stem Cells From Adult Human Fibroblasts by Defined Factors.
942 *Cell*. **131**, 861-72 (2007).

943 14. Hu, B.Y., Du, Z.W., Zhang, S.C. Differentiation of Human Oligodendrocytes From Pluripotent Stem Cells.
944 *Nat Protoc*. **4**, 1614-22 (2009).

945 15. Haston, K.M., Finkbeiner, S. Clinical Trials in a Dish: The Potential of Pluripotent Stem Cells to Develop
946 Therapies for Neurodegenerative Diseases. *Annu Rev Pharmacol Toxicol*. **56**, 489-510 (2016).

947 16. Abud, E.M, *et al*. iPSC-Derived Human Microglia-like Cells to Study Neurological Diseases. *Neuron*. **94**,
948 278-293 (2017).

949 17. de Rus Jacquet, A. Preparation and Co-Culture of iPSC-Derived Dopaminergic Neurons and Astrocytes. *Curr*
950 *Protoc Cell Biol*. **85**, e98 (2019).

951 18. Lanko, K, *et al*. Replication of the Zika Virus in Different iPSC-derived Neuronal Cells and Implications to
952 Assess Efficacy of Antivirals. *Antiviral Res*. **145**, 82-86 (2017).

953 19. Fujimori, K, *et al*. Modeling Sporadic ALS in iPSC-derived Motor Neurons Identifies a Potential Therapeutic
954 Agent. *Nat Med*. **24**, 1579-1589 (2018).

955 20. Lebedeva, O.S. & Lagarkova, M.A. Pluripotent Stem Cells for Modelling and Cell Therapy of Parkinson's
956 Disease. *Biochemistry (Mosc)*. **83**, 1046-1056 (2018).

957 21. Monzio Compagnoni, G, *et al*. Mitochondrial Dysregulation and Impaired Autophagy in iPSC-Derived
958 Dopaminergic Neurons of Multiple System Atrophy. *Stem Cell Reports*. **11**, 1185-1198 (2018).

959 22. Huang, B, *et al*. Inflammatory Responses to a Pathogenic West Nile Virus Strain. *BMC Infect Dis*. **19**, 912
960 (2019).

961 23. Penney, J., Ralvenius, W.T., Tsai, L.H. Modeling Alzheimer's Disease With iPSC-derived Brain Cells. *Mol*
962 *Psychiatry*. **25**, 148-167 (2020).

963 24. Csobonyeiova, M., Polak, S., Danisovic, L. Recent Overview of the Use of iPSCs Huntington's Disease
964 Modeling and Therapy. *Int J Mol Sci*. **21**, 2239 (2020).

965 25. Teque, F, *et al*. Genetically-edited Induced Pluripotent Stem Cells Derived From HIV-1-infected Patients on
966 Therapy Can Give Rise to Immune Cells Resistant to HIV-1 Infection. *AIDS*. **34**, 1141-114 (2020).

967 26. Pampaloni, F., Reynaud, E.G., Stelzer, E.H. The Third Dimension Bridges the Gap Between Cell Culture and
968 Live Tissue. *Nat Rev Mol Cell Biol*. **8**, 839-45 (2007).

969 27. Topol, A., Tran, N.N., Brennand, K.J. A Guide to Generating and Using hiPSC Derived NPCs for the Study of
970 Neurological Diseases. *J Vis Exp*. **96**, e52495 (2015).

971 28. Zhou, S, *et al*. Neurosphere Based Differentiation of Human iPSC Improves Astrocyte Differentiation. *Stem*
972 *Cells Int*. **2016**, 4937689 (2016).

973 29. Hofrichter, M, *et al*. Comparative Performance Analysis of Human iPSC-derived and Primary Neural
974 Progenitor Cells (NPC) Grown as Neurospheres in Vitro. *Stem Cell Res*. **25**, 72-82 (2017).

975 30. Ostenfeld, T, *et al*. Regional Specification of Rodent and Human Neurospheres. *Brain Res Dev Brain Res*.
976 **134**, 43-55 (2002).

977 31. Parmar, M., Skogh, C., Björklund, A., Campbell, K. Regional Specification of Neurosphere Cultures Derived
978 From Subregions of the Embryonic Telencephalon. *Mol Cell Neurosci*. **21**, 645-56 (2002).

979 32. Jensen, J.B. & Parmar, M. Strengths and limitations of the neurosphere culture system. *Mol Neurobiol*. **34**,
980 153-161 (2006).

981 33. Garcez, P.P, *et al*. Zika virus impairs growth in human neurospheres and brain organoids. *Science.* **352**, 816-
982 818 (2016).

983 34. Garcez, P.P, *et al*. Zika virus disrupts molecular fingerprinting of human neurospheres. *Sci Rep*. **7**, 40780
984 (2017).

985 35. D'Aiuto, L, *et al*. Generation of three-dimensional human neuronal cultures: application to modeling CNS viral
986 infections. *Stem Cell Res Ther*. **9**, 134 (2018).

987 36. Gribkoff, V.K. & Kaczmarek, L.K. The need for new approaches in CNS drug discovery: Why drugs have
988 failed, and what can be done to improve outcomes. *Neuropharmacology*. **120**, 11-19 (2017).

989 37. Danon, J.J., Reekie, T.A., Kassiou, M. Challenges and Opportunities in Central Nervous System Drug
990 Discovery. *Trends in Chemistry*. **1**, P612-624 (2019).

991 38. Phinney, D.G. & Pittenger, M.F. Concise Review: MSC-Derived Exosomes for Cell-Free Therapy. *Stem Cells*.
992 **35**, 851-858 (2017).

993 39. van Niel, G., D'Angelo, G., Raposo, G. Shedding light on the cell biology of extracellular vesicles. *Nat Rev*
994 *Mol Cell Biol*. **19**, 213-228 (2018).

995 40. Zaborowski, M.P., Balaj, L., Breakefield, X.O., Lai, C.P. Extracellular Vesicles: Composition, Biological
996 Relevance, and Methods of Study. *Bioscience*. **65**, 783-797 (2015).

997 41. Deng, H, *et al*. Lipid, Protein, and MicroRNA Composition Within Mesenchymal Stem Cell-Derived
998 Exosomes. *Cell Reprogram*. **20**, 178-186 (2018).

999 42. Luarte, A., Bátiz, L.F., Wyneken, U., Lafourcade, C. Potential Therapies by Stem Cell-Derived Exosomes in
1000 CNS Diseases: Focusing on the Neurogenic Niche. *Stem Cells Int*. **2016**, 5736059 (2016).

1001 43. Taheri, B, *et al*. Induced pluripotent stem cell-derived extracellular vesicles: A novel approach for cell-free
1002 regenerative medicine. *J Cell Physiol*. **234**, 8455-8464 (2019).

1003 44. Koniusz, S, *et al*. Extracellular Vesicles in Physiology, Pathology, and Therapy of the Immune and Central
1004 Nervous System, with Focus on Extracellular Vesicles Derived from Mesenchymal Stem Cells as Therapeutic
1005 Tools. *Front Cell Neurosci*. **10**, 109 (2016).

1006 45. Keshtkar, S., Azarpira, N., Ghahremani, M.H. Mesenchymal stem cell-derived extracellular vesicles: novel
1007 frontiers in regenerative medicine. *Stem Cell Res Ther*. **9**, 63 (2018).

1008 46. Branscome, H, *et al*. Use of Stem Cell Extracellular Vesicles as a "Holistic" Approach to CNS Repair. *Front*
1009 *Cell Dev Biol*. **8**, 455 (2020).

1010 47. Galieva, L.R., James, V., Mukhamedshina, Y.O., Rizvanov, A.A. Therapeutic Potential of Extracellular
1011 Vesicles for the Treatment of Nerve Disorders. *Front Neurosci*. **13**, 163 (2019).

1012 48. Mesci, P, *et al*. Blocking Zika virus vertical transmission. *Sci Rep*. **8**,1218 (2018).

1013 49. Ye, L, *et al*. Blood cell-derived induced pluripotent stem cells free of reprogramming factors generated by
1014 Sendai viral vectors. *Stem Cells Transl Med*. **2**, 558-566 (2013).

1015 50. D'Aiuto, L, *et al*. Large-scale generation of human iPSC-derived neural stem cells/early neural progenitor cells
1016 and their neuronal differentiation. *Organogenesis*. **10**, 365-377 (2014).

1017 51. Chandrasekaran, A, *et al*. Comparison of 2D and 3D neural induction methods for the generation of neural
1018 progenitor cells from human induced pluripotent stem cells. *Stem Cell Res*. **25**, 139-151 (2017).

1019 52. Kang, S, *et al*. Characteristic analyses of a neural differentiation model from iPSC-derived neuron according to
1020 morphology, physiology, and global gene expression pattern. *Sci Rep*. **7**, 12233 (2017).

1021 53. Bianchi, F, *et al*. Rapid and efficient differentiation of functional motor neurons from human iPSC for neural
1022 injury modelling. *Stem Cell Res*. **32**, 126-134 (2018).

1023 54. Simão, D, *et al*. Recapitulation of Human Neural Microenvironment Signatures in iPSC-Derived NPC 3D
1024 Differentiation. *Stem Cell Reports*. **11**, 552-564 (2018).

1025 55. Blumberg, B.M., Gelbard, H.A., Epstein, L.G. HIV-1 infection of the developing nervous system: central role
1026 of astrocytes in pathogenesis. *Virus Res*. **32**, 253-267 (1994).

1027 56. Gray, L.R, *et al*. Is the central nervous system a reservoir of HIV-1?. *Curr Opin HIV AIDS*. **9**, 552-558 (2014).

1028 57. Li, G.H., Henderson L., Nath, A. Astrocytes as an HIV Reservoir: Mechanism of HIV Infection. *Curr HIV*
1029 *Res*. **14**, 373-381 (2016).

1030 58. Joseph, S.B., Arrildt, K.T., Sturdevant, C.B., Swanstrom, R. HIV-1 target cells in the CNS. *J Neurovirol*. **21**,
1031 276-289 (2015).

1032 59. Rojas-Celis, V., Valiente-Echeverría, F., Soto-Rifo, R., Toro-Ascuy, D. New Challenges of HIV-1 Infection:
1033 How HIV-1 Attacks and Resides in the Central Nervous System. *Cells*. **8**, 1245 (2019).

1034 60. Wallet, C, *et al*. Microglial Cells: The Main HIV-1 Reservoir in the Brain. *Front Cell Infect Microbiol*. **9**, 362
1035 (2019).

1036 61. Lutgen, V, *et al*. HIV infects astrocytes in vivo and egresses from the brain to the periphery. *PLoS Pathog*. **16**,
1037 e1008381 (2020).

1038 62. Levin, M.C. & Jacobson, S. HTLV-I associated myelopathy/tropical spastic paraparesis (HAM/TSP): a chronic
1039 progressive neurologic disease associated with immunologically mediated damage to the central nervous system. *J*
1040 *Neurovirol*. **3**,126-140 (1997).

1041 63. Grant, C *et al*. Human T cell leukemia virus type I and neurologic disease: events in bone marrow, peripheral
1042 blood, and central nervous system during normal immune surveillance and neuroinflammation. *J Cell Physiol*. **190**,
1043 133-59 (2002).

1044 64. Lepoutre, V., Jain, P., Quann, K., Wigdahl, B., Khan, Z.K. Role of resident CNS cell populations in HTLV-1-
1045 associated neuroinflammatory disease. *Front Biosci (Landmark Ed)*. **14**, 1152-1168 (2009).

1046 65. Nozuma, S. & Jacobson, S. Neuroimmunology of Human T-Lymphotropic Virus Type 1-Associated
1047 Myelopathy/Tropical Spastic Paraparesis. *Front Microbiol*. **10**, 885 (2019).

1048 66. Iordanskiy, S, *et al*. Therapeutic doses of irradiation activate viral transcription and induce apoptosis in HIV-1
1049 infected cells. *Virology*. **485**, 1-15 (2015).

1050 67. Iordanskiy, S. & Kashanchi, F. Potential of Radiation-Induced Cellular Stress for Reactivation of Latent HIV-1
1051 and Killing of Infected Cells. *AIDS Res Hum Retroviruses*. **32**,120-124 (2016).

1052 68. Pinto, D.O, *et al*. HTLV-1 Extracellular Vesicles Promote Cell-to-Cell Contact. *Front Microbiol*. **10**, 2147
1053 (2019).

1054 69. Gill, P.S, *et al*. Treatment of adult T-cell leukemia-lymphoma with a combination of interferon alfa and
1055 zidovudine. *N Engl J Med*. **332**, 1744-1748 (1995).

1056 70. Hermine, O, *et al*. Brief report: treatment of adult T-cell leukemia-lymphoma with zidovudine and interferon
1057 alfa. *N Engl J Med*. **332**, 1749-1751 (1995).

1058 71. Pasquier, A, *et al*. How to Control HTLV-1-Associated Diseases: Preventing de Novo Cellular Infection Using
1059 Antiviral Therapy. *Front Microbiol*. **9**, 278 (2018).

1060 72. Branscome, H, *et al*. Stem Cell Extracellular Vesicles and their Potential to Contribute to the Repair of
1061 Damaged CNS Cells. *J Neuroimmune Pharmacol*. **2019**, 10.1007/s11481-019-09865-y (2019).

1062 73. Heinemann, M.L. & Vykoukal, J. Sequential Filtration: A Gentle Method for the Isolation of Functional
1063 Extracellular Vesicles. *Methods Mol Biol*. **1660**, 33-41 (2017).

1064 74. Busatto, S, *et al*. Tangential Flow Filtration for Highly Efficient Concentration of Extracellular Vesicles from
1065 Large Volumes of Fluid. *Cells*. **7**, 273 (2018).

1066 75. Haraszti, R.A, *et al*. Exosomes Produced from 3D Cultures of MSCs by Tangential Flow Filtration Show
1067 Higher Yield and Improved Activity. *Mol Ther*. **26**, 2838-2847 (2018).

1068 76. El Baradie, K.B.Y, *et al*. Freeze-Dried Extracellular Vesicles From Adipose-Derived Stem Cells Prevent
1069 Hypoxia-Induced Muscle Cell Injury. *Front Cell Dev Biol*. **8**, 181 (2020).

1070 77. Larsen, P.H., Wells, J.E., Stallcup, W.B., Opdenakker, G., Yong, V.W. Matrix metalloproteinase-9 facilitates
1071 remyelination in part by processing the inhibitory NG2 proteoglycan. *J Neurosci*. **23**, 11127-11135 (2003).

1072

1073 78. Reinhard, S.M., Razak, K., Ethell, I.M. A delicate balance: role of MMP-9 in brain development and
1074 pathophysiology of neurodevelopmental disorders. *Front Cell Neurosci*. **9**, 280 (2015).

1075 79. Toth, M. & Fridman, R. Assessment of Gelatinases (MMP-2 and MMP-9 by Gelatin Zymography. *Methods*
1076 *Mol Med*. **57**, 163-174 (2001).

1077 80. Tajhya, R.B., Patel, R.S., Beeton, C. Detection of Matrix Metalloproteinases by Zymography. *Methods Mol*
1078 *Biol*. **1579**, 231-244 (2017).

1079 81. Chang, C.L, *et al*. Adipose-derived mesenchymal stem cell-derived exosomes markedly protected the brain
1080 against sepsis syndrome induced injury in rat. *Am J Transl Res*. **11**, 3955-3971 (2019).

1081 82. Kumar, P, *et al*. Neuroprotective effect of placenta-derived mesenchymal stromal cells: role of exosomes.
1082 *FASEB J*. **33**, 5836-5849 (2019).

1083 83. Liu, W, *et al*. Exosomes Derived from Bone Mesenchymal Stem Cells Repair Traumatic Spinal Cord Injury by
1084 Suppressing the Activation of A1 Neurotoxic Reactive Astrocytes. *J Neurotrauma*. **36**, 469-484 (2019).

1085 84. Guo, H, *et al*. Bone marrow mesenchymal stem cells-derived exosomes improve injury of hippocampal neurons
1086 in rats with depression by upregulating microRNA-26a expression. *Int Immunopharmacol*. **82**, 106285 (2020).

1087 85. Chen, H.X, *et al*. Exosomes derived from mesenchymal stem cells repair a Parkinson's disease model by
1088 inducing autophagy. *Cell Death Dis*. **11**, 288 (2020).

1089 86. Liu, C.Y, *et al*. Effect of exosomes from adipose-derived stem cells on the apoptosis of Schwann cells in
1090 peripheral nerve injury. *CNS Neurosci Ther*. **26**, 189-196 (2020).

1091 87. Long, Q, *et al*. Intranasal MSC-derived A1-exosomes ease inflammation, and prevent abnormal neurogenesis
1092 and memory dysfunction after status epilepticus. *Proc Natl Acad Sci U S A*. **114**, E3536-E3545 (2017).

1093 88. Ding, M, *et al*. Exosomes Isolated From Human Umbilical Cord Mesenchymal Stem Cells Alleviate
1094 Neuroinflammation and Reduce Amyloid-Beta Deposition by Modulating Microglial Activation in Alzheimer's
1095 Disease. *Neurochem Res*. **43**, 2165-2177 (2018).

1096 89. Feng, N., Jia, Y., Huang, X. Exosomes from adipose-derived stem cells alleviate neural injury caused by
1097 microglia activation via suppressing NF-kB and MAPK pathway. *J Neuroimmunol*. **334**, 576996 (2019).

1098 90. Ni, H, *et al*. Exosomes Derived From Bone Mesenchymal Stem Cells Ameliorate Early Inflammatory
1099 Responses Following Traumatic Brain Injury. *Front Neurosci*. **13**,14 (2019).

1100 91. Sun, G, *et al*. hucMSC derived exosomes promote functional recovery in spinal cord injury mice via
1101 attenuating inflammation. *Mater Sci Eng C Mater Biol Appl*. **89**,194-204 (2018).

1102 92. Thomi, G., Surbek, D., Haesler, V., Joerger-Messerli, M., Schoeberlein, A. Exosomes derived from umbilical
1103 cord mesenchymal stem cells reduce microglia-mediated neuroinflammation in perinatal brain injury. *Stem Cell Res*
1104 *Ther*. **10**, 105 (2019).

1105 93. Ching, R.C., Wiberg, M., Kingham, P.J. Schwann cell-like differentiated adipose stem cells promote neurite
1106 outgrowth via secreted exosomes and RNA transfer. *Stem Cell Res Ther*. **9**, 266 (2018).

1107 94. Qiu, G, *et al.* Mesenchymal stem cell-derived extracellular vesicles affect disease outcomes via transfer of
1108 microRNAs. *Stem Cell Res Ther*. **9**, 320 (2018).

1109 95. Bodart-Santos, V, *et al*. Extracellular vesicles derived from human Wharton's jelly mesenchymal stem cells
1110 protect hippocampal neurons from oxidative stress and synapse damage induced by amyloid-β oligomers. *Stem Cell*
1111 *Res Ther*. **10**, 332 (2019).

1112 96. Yin, K., Wang, S. Zhao, R.C. Exosomes from mesenchymal stem/stromal cells: a new therapeutic paradigm.
1113 *Biomark Res*. **7**, 8 (2019).

1114 97. Shojaati, G, *et al*. Mesenchymal Stem Cells Reduce Corneal Fibrosis and Inflammation via Extracellular
1115 Vesicle-Mediated Delivery of miRNA. *Stem Cells Transl Med*. **8**, 1192-1201 (2019).

1116 98. Baglio, S.R, *et al*. Human bone marrow- and adipose-mesenchymal stem cells secrete exosomes enriched in
1117 distinctive miRNA and tRNA species. *Stem Cell Res Ther*. **6**, 127 (2015).

1118 99. Deng, H, *et al*. Lipid, Protein, and MicroRNA Composition Within Mesenchymal Stem Cell-Derived
1119 Exosomes. *Cell Reprogram*. **20**, 178-186 (2018).

1120 100. Ferguson, S.W, *et al*. The microRNA regulatory landscape of MSC-derived exosomes: a systems view. *Sci*
1121 *Rep*. **8**, 1419 (2018).

1122 101. Kaur, S, *et al*. Small non-coding RNA landscape of extracellular vesicles from human stem cells. *Sci Rep*. **8**,
1123 15503 (2018).

1124 102. Cole, J.L. Activation of PKR: an open and shut case? *Trends Biochem Sci*. **32**, 57-62 (2007).

1125 103. Husain, B., Mukerji, I., Cole, J.L. Analysis of high-affinity binding of protein kinase R to double-stranded
1126 RNA. *Biochemistry*. **51**, 8764-8770 (2012).

1127 104. Narayanan, A, *et al*. Exosomes derived from HIV-1-infected cells contain trans-activation response element
1128 RNA. *J Biol Chem*. **288**, 20014-33 (2013).

1129 105. Sampey, G.C, *et al*. Exosomes from HIV-1-infected Cells Stimulate Production of Pro-inflammatory
1130 Cytokines through Trans-activating Response (TAR) RNA. *J Biol Chem*. **291**, 1251-1266 (2016).

1131 106. Barclay, R.A, *et al*. Exosomes from uninfected cells activate transcription of latent HIV-1. *J Biol Chem*. **292**,
1132 14764 (2017).

1133 107. Barclay, R.A, *et al*. An Omics Approach to Extracellular Vesicles from HIV-1 Infected Cells. *Cells*. **8**, 787
1134 (2019).

1135 108. Roberts, E.S., Masliah, E., Fox, H.S. CD163 identifies a unique population of ramified microglia in HIV
1136 encephalitis (HIVE). *J Neuropathol Exp Neurol*. **63**, 1255-1264 (2004).

1137 109. Korzhevskii, D.E. & Kirik, O.V. Brain Microglia and Microglial Markers. *Neurosci Behav Physi*. **46**, 284-
1138 290 (2016).

1139 110. Hopperton, K.E., Mohammad, D., Trépanier, M.O., Giuliano, V., Bazinet, R.P. Markers of microglia in post-
1140 mortem brain samples from patients with Alzheimer's disease: a systematic review. *Mol Psychiatry*. **23**, 177-198
1141 (2018).

1142 111. Zrzavy, T, *et al*. Pro-inflammatory activation of microglia in the brain of patients with sepsis. *Neuropathol*
1143 *Appl Neurobiol*. **45**, 278-290 (2019).

1144 112. DePaula-Silva, A.B, *et al*. Differential transcriptional profiles identify microglial- and macrophage-specific
1145 gene markers expressed during virus-induced neuroinflammation. *J Neuroinflammation*. **16**, 152 (2019).

1146 113. Guillemin, G.J. & Brew, B.J. Microglia, macrophages, perivascular macrophages, and pericytes: a review of
1147 function and identification. *J Leukoc Biol*. **75**, 388-397 (2004).

1148 114. Kaul, M., Zheng, J., Okamoto, S., Gendelman, H.E., Lipton, S.A. HIV-1 infection and AIDS: consequences
1149 for the central nervous system. *Cell Death Differ*. **12 Suppl 1**, 878-892 (2005).

1150 115. Nuovo, G.J. & Alfieri, M.L. AIDS dementia is associated with massive, activated HIV-1 infection and
1151 concomitant expression of several cytokines. *Mol Med*. **2**, 358-366 (1996).

1152 116. Bagasra, O, *et al*. Cellular reservoirs of HIV-1 in the central nervous system of infected individuals:
1153 identification by the combination of in situ polymerase chain reaction and immunohistochemistry. *AIDS*. **10**, 573-
1154 585 (1996).

1155 117. Takahashi, K, *et al*. Localization of HIV-1 in human brain using polymerase chain reaction/in situ
1156 hybridization and immunocytochemistry. *Ann Neurol*. **39**, 705-711 (1996).

1157 118. Chompre, G, *et al*. Astrocytic expression of HIV-1 Nef impairs spatial and recognition memory. *Neurobiol*
1158 *Dis*. **49**, 128-136 (2013).

1159 119. O'Doherty, U., Swiggard, W.J., Jeyakumar, D., McGain, D., Malim, M.H. A sensitive, quantitative assay for
1160 human immunodeficiency virus type 1 integration. *J Virol*. **76**, 10942-10950 (2002).

1161 120. Yu, J.J, *et al*. A more precise HIV integration assay designed to detect small differences finds lower levels of
1162 integrated DNA in HAART treated patients. *Virology*. **379**, 78-86 (2008).

1163 121. Liszewski, M.K., Yu, J.J., O'Doherty, U. Detecting HIV-1 integration by repetitive-sampling Alu-gag PCR.
1164 *Methods*. **47**, 254-260 (2009).

1165 122. Pinzone, M.R. & O'Doherty, U. Measuring integrated HIV DNA ex vivo and in vitro provides insights about
1166 how reservoirs are formed and maintained. *Retrovirology*. **15**, 22 (2018).

1167 123. Eng, L.F., Ghirnikar, R.S., Lee, Y.L. Glial fibrillary acidic protein: GFAP-thirty-one years (1969-2000).
1168 *Neurochem Res*. **25**, 1439-1451 (2000).

1169 124. Sofroniew, M.V. & Vinters, H.V. Astrocytes: biology and pathology. *Acta Neuropathol*. **119**, 7-35 (2010).

1170 125. Zhou, B.Y., Liu, Y., Kim, Bo, Xiao, Y., He, J.J. Astrocyte activation and dysfunction and neuron death by
1171 HIV-1 Tat expression in astrocytes. *Mol Cell Neurosci*. **27**, 296-305 (2004).

1172 126. Bell, J.E., Anthony, I.C., Simmonds, P. Impact of HIV on regional & cellular organisation of the brain. *Curr*
1173 *HIV Res*. **4**, 249-257 (2006).

1174 127. Zou, W, *et al*. Involvement of p300 in constitutive and HIV-1 Tat-activated expression of glial fibrillary acidic
1175 protein in astrocytes. *Glia*. **58**, 1640-1648 (2010).

1176 128. Teyssier, F., Bay, J.O., Dionet, C., Verrelle, P. Régulation du cycle cellulaire des cellules exposées aux
1177 radiations ionisantes [Cell cycle regulation after exposure to ionizing radiation]. *Bull Cancer*. **86**, 345-357 (1999).

1178 129. DeMarino, C, *et al*. Antiretroviral Drugs Alter the Content of Extracellular Vesicles from HIV-1-Infected
1179 Cells. *Sci Rep*.. **8**, 7653 (2018).

1180 130. Pleet, M.L, *et al*. Ebola Virus VP40 Modulates Cell Cycle and Biogenesis of Extracellular Vesicles. *J Infect*
1181 *Dis*. **218 (suppl_5)**, S365-S387 (2018).

1182 131. DeMarino, C, *et al*. Purification of High Yield Extracellular Vesicle Preparations Away from Virus. *J Vis*
1183 *Exp*. **151**, 10.3791/59876 (2019).

1184 132. Gorabi, A.M, *et al*. The Therapeutic Potential of Mesenchymal Stem Cell-Derived Exosomes in Treatment of
1185 Neurodegenerative Diseases. *Mol Neurobiol*. **56**, 8157-8167 (2019).

1186 133. Kaufmann, S.H., Desnoyers, S., Ottaviano, Y., Davidson, N.E., Poirier, G.G. Specific proteolytic cleavage of
1187 poly(ADP-ribose) polymerase: an early marker of chemotherapy-induced apoptosis. *Cancer Res*. **53**, 3976-3985
1188 (1993).

1189 134. Soldani, C. & Scovassi, A.I. Poly(ADP-ribose) polymerase-1 cleavage during apoptosis: an update. *Apoptosis*.
1190 **7**, 321-328 (2002).

1191 135. Lambert, P.F., Kashanchi, F., Radonovich, M.F., Shiekhattar, R., Brady, J.N. Phosphorylation of p53 serine
1192 15 increases interaction with CBP. *J Biol Chem*. **273**, 33048-33053 (1998).

1193 136. Loughery, J., Cox, M., Smith, L.M., Meek, D.W. Critical role for p53-serine 15 phosphorylation in
1194 stimulating transactivation at p53-responsive promoters. *Nucleic Acids Res*. **42**, 7666-7680 (2014).

1195 137. Yogosawa, S. & Yoshida, K. Tumor suppressive role for kinases phosphorylating p53 in DNA damage-
1196 induced apoptosis. *Cancer Sci*. **109**, 3376-3382 (2018).

1197 138. Cohen, G.M. Caspases: the executioners of apoptosis. *Biochem J*. **326 ( Pt 1)(Pt 1)**, 1-16 (1997).

1198 139. Porter, A.G. & Jänicke, R.U. Emerging roles of caspase-3 in apoptosis. *Cell Death Differ*. **6**, 99-104 (1999).

1199 140. Zhang, J, *et al*. Exosome and exosomal microRNA: trafficking, sorting, and function. *Genomics Proteomics*
1200 *Bioinformatics*. **13**, 17-24 (2015).

1201 141. Hewson, C., Capraro, D., Burdach, J., Whitaker, N., Morris, K.V. Extracellular vesicle associated long non-
1202 coding RNAs functionally enhance cell viability. *Noncoding RNA Res*. **1**, 3-11 (2016).

1203 142. Yu, X., Odenthal, M., Fries, J.W. Exosomes as miRNA Carriers: Formation-Function-Future. *Int J Mol Sci*.
1204 **17**, 2028 (2016).

1205 143. Kelemen, E., Danis, J., Göblös, A., Bata-Csörgő, Z., Széll, M. Exosomal long non-coding RNAs as
1206 biomarkers in human diseases. *EJIFCC*. **30**, 224-236 (2019).

1207 144. Abramowicz, A. & Story, M.D. The Long and Short of It: The Emerging Roles of Non-Coding RNA in Small
1208 Extracellular Vesicles. *Cancers (Basel)*. **12**, 1445 (2020).

1209 145. Groot, M. & Lee, H. Sorting Mechanisms for MicroRNAs into Extracellular Vesicles and Their Associated
1210 Diseases. *Cells*. **9**, 1044 (2020).

1211 146. Santer, L., Bär, C., Thum, T. Circular RNAs: A Novel Class of Functional RNA Molecules with a Therapeutic
1212 Perspective. *Mol Ther*. **27**, 1350-1363 (2019).

1213 147. Zhong, Y, *et al*. Circular RNAs function as ceRNAs to regulate and control human cancer progression. *Mol*
1214 *Cancer*. **17**, 79 (2018).

1215 148. Ali, S.A, *et al*. Genetic characterization of HIV type 1 Nef-induced vesicle secretion. *AIDS Res Hum*
1216 *Retroviruses*. **26**, 173-192 (2010).

1217 149. Urbanelli, L, *et al*. The Role of Extracellular Vesicles in Viral Infection and Transmission. *Vaccines (Basel)*.
1218 **7**, 102 (2019).

1219 150. Martin, M. Cutadapt removes adapter sequences from high-throughput sequencing reads. *EMBnet.journal*.
1220 **17.1** (2011).

1221 151. Kim, D, *et al*. TopHat2: accurate alignment of transcriptomes in the presence of insertions, deletions and gene
1222 fusions. *Genome Biol*. **14**, R36 (2013).

1223 152. Langmead, B. & Salzberg, S.L. Fast gapped-read alignment with Bowtie 2. *Nat Methods*. **9**, 357-359 (2012).

1224 153. Pertea, M, *et al*. StringTie enables improved reconstruction of a transcriptome from RNA-seq reads. *Nat*
1225 *Biotechnol*. **33**, 290-295 (2015).

1226 154. Frazee, A.C, *et al*. Ballgown bridges the gap between transcriptome assembly and expression analysis. *Nat*
1227 *Biotechnol*. **33**, 243-246 (2015).

1228 155. Gruber, A.R., Lorenz, R., Bernhart, S.H., Neuböck, R., Hofacker, I.L. The Vienna RNA websuite. *Nucleic*
1229 *Acids Res*. **36(Web Server issue)**, W70-W74 (2008).

156. Zuker, M. & Stiegler, P. Optimal computer folding of large RNA sequences using thermodynamics and auxiliary information. *Nucleic Acids Res*. **9**, 133-148 (1981).

157. Mathews, D.H., Sabina, J., Zuker, M., Turner, D.H. Expanded sequence dependence of thermodynamic parameters improves prediction of RNA secondary structure. *J Mol Biol*. **288**, 911-940 (1999).

1262 **Figure Legends**

1263 **Figure 1. Generation and characterization of NPC-derived neurospheres. (a)** General workflow and
1264 approximate timeline associated with the development of neurospheres using human somatic cells as the starting
1265 material. **(b)** Representative phase contrast images show the appearance and morphology of NPC-derived
1266 neurospheres during the course of the differentiation period (weeks 12 through 14). Scale bar = 100 µm. **(c)**
1267 Average diameter (µm) of NPC-derived neurospheres during the course of the differentiation period. n=3. **(d)** ICC
1268 staining of differentiated neurospheres shows the relative expression of neurons (FOXA2), astrocytes (GFAP),
1269 and microglia-like cells (CD163, Iba-1). Nuclei were counter-stained with DAPI. Scale bar = 100 µm.

1270 **Figure 2. HIV-1 infection of NPC-derived neurospheres.** Differentiated neurospheres were exposed to dual-
1271 tropic HIV-1 89.6, JR-CSF, and CHO40 (MOI:10) for a period of seven days. **(a)** Western blot was performed to
1272 examine the relative expression of Pr55, p24, and Nef in HIV-1 89.6 neurospheres cultured with or without cART
1273 (lamivudine, tenofovir disoproxil fumarate, emtricitabine, indinavir). **(b)** RT-qPCR was performed to examine the
1274 relative copy numbers of TAR and *env* RNA in HIV-1 89.6 neurospheres with or without cART. n=3. *$p < 0.05$
1275 relative to HIV-1 alone. **(c)** Western blot was performed to compare the relative expression of p24 in HIV-1 89.6,
1276 JR-CSF, and CHO40 infected neurospheres. **(d)** Neurospheres were gently disaggregated and IP was performed
1277 using antibodies specific for astrocytes (GFAP), microglia-like cells (Integrin αm/CD11b), neurons (GAD65), and
1278 NSCs( SOX2) followed by direct PCR to quantify copies of TAR DNA in different subpopulations of HIV-1 89.6,
1279 JR-CSF, and CHO40-infected neurospheres. n=3. * $p < 0.05$.

1280 **Figure 3. Expression of differentiated cells in HIV-1 and HTLV-1 infected neurospheres**. **(a)**
1281 Differentiated neurospheres were exposed to dual-tropic HIV-1 89.6 with or without cART (lamivudine, tenofovir
1282 disoproxil fumarate, emtricitabine, indinavir), or co-cultured with HTLV-1 infected cells with or without IFN/AZT
1283 treatment for a period of seven days. Western blot was performed to examine the relative expression of CNS-
1284 specific cell types including microglia-like cells, astrocytes, neurons (dopaminergic, GABAergic, glutamatergic),
1285 and NSCs. **(b)** Western blot was performed to examine the relative expression of Tax and p19 in neurospheres co-
1286 cultured with HTLV-1 infected cells with or without IFN/AZT treatment. **(c)** RT-qPCR was performed to quantify
1287 the copy numbers of *tax*, *env*, and *hbz* RNA in neurospheres co-cultured with HTLV-1 infected cells with or without
1288 IFN/AZT treatment. n=3. *** $p < 0.0001$.

1289 **Figure 4. Functional effects of stem cell EVs on HIV-1 infected neurospheres.** EVs from stem cells as well as
1290 A549 cells were concentrated using TFF. Data from A549 EVs is included to serve as a control for NTA analysis
1291 and EV uptake. **(a)** NTA was performed and representative histograms from three independent measurements show
1292 the relative size distribution of each EV prep. **(b)** EVs were fluorescently labeled with BODIPY™ 493/503. After
1293 removal of excess dye, EVs were added to differentiated neurospheres and allowed to incubate. Representative

1294 phase contrast and fluorescent images show the relative uptake of EVs on Days 1 and 8. Scale bar = 100 μm. **(c)**
1295 Differentiated neurospheres were exposed to dual-tropic HIV-1 89.6 with or without cART. cART treated cells
1296 were also treated with either iPSC or MSC EVs. Cultures were maintained for seven days. Western blot was
1297 performed to evaluate the relative expression of PARP-1, p53, p-p53 (ser-15), p-p21 (ser-146), and Caspase-3) or
1298 **(d)** TNFα, IL-8, and IL-1β.

1299 **Figure 5. RNA analysis of EVs**. RNA sequencing of EV-associated lncRNAs was performed. **(a)** Percentages of
1300 transcripts mapping to either exons, introns, or intergenic regions are shown. **(b)** Chromosome maps show the
1301 relative density distribution of EV-associated transcripts. **(c)** Percentages of non-annotated transcripts. Transcripts
1302 that were not annotated in genome databases were designated as novel transcripts according to the following class
1303 codes: i = transfrag falling within a reference intron; j = potentially novel isoform with at least one splice junction
1304 shared with a reference transcript; o = generic exonic overlap with a reference transcript; u = unknown intergenic
1305 transcript; x = exonic overlap with reference on the opposite strand. **(d)** Heat maps comparing lncRNA transcripts
1306 between iPSC and A549 EVs (left panel) and MSC and A549 EVs (right panel). **(e)** Volcano plots displaying the
1307 differentially expressed transcripts between iPSC and A549 EVs (left panel) and MSC and A549 EVs (right panel).
1308 Significantly regulated transcripts are annotated with their corresponding gene ID.

1309 **Figure 6. RNA pulldown assay. (a)** The secondary structures of lncRNAs ADIRF-AS1 and AC120498.9
1310 contained continuous stretches of dsRNA ≥ 30 base pairs in length. For reference, the corresponding regions are
1311 enclosed in black boxes. **(b)** Biotin-conjugated synthetic RNA sequences corresponding to the sequences of interest
1312 were incubated with SHSY5Yextract. Western blot was performed to assess the expression of different RNA
1313 binding proteins (PKR, Dicer, ADAR1). **(c)** SHSY5Y cells were exposed to EVs from HIV-1 infected cells with or
1314 without treatment of stem cell EVs. Stem cell EVs were exposed to UV(C) to inactivate EV-associated RNAs.
1315 Representative images show the appearance and morphology of cells after 8 days in culture. Scale bar = 200 μm.
1316 **(d)** Cell viability was quantified via CellTiter-Glo. n=3. *$p < 0.05$ relative to U1 cART EVs.

1317 **Supplemental Figure 1.** ICC staining of 2D cultures of differentiated NPCs. NPCs were incubated with
1318 antibodies against immature neurons (Tuj1), dopaminergic neurons (TH), and astrocytes (GFAP). Phase contrast
1319 images show the morphology of differentiated NPCs. Fluorescent imaging shows the relative expression of Tuj1,
1320 TH, and GFAP. Nuclei were counterstained with DAPI. Scale bar = 400 μm**.**

1321 **Supplementary Figure 2. (a)** EVs were fluorescently labeled with SYTO® RNASelect Green Fluorescent Stain.
1322 After removal of excess dye, EVs were added to differentiated neurospheres and allowed to incubate.
1323 Representative phase contrast and fluorescent images show the relative uptake of EVs on Days 1 and 8**.** Scale bar =
1324 100 μm**. (b)** Western blot was performed to evaluate the relative expression of MMP9 in each EV preparation. **(c)**
1325 Gelatin zymography was performed to examine the proteolytic activity of EVs. Imaging of the stained gel shows

areas of gelatin degradation corresponding to both MMP9 and MMP2 activity.

**Supplementary Figure 3.** Differentiated neurospheres were exposed to HIV-1 (JR-CSF and CHO40; MOI:10) with or without cART (lamivudine, tenofovir disoproxil fumarate, emtricitabine, indinavir) for a period of seven days. Western blot was performed to assess the relative expression of TNFα, IL-8, and IL-1β.

**Supplementary Figure 4**. **(a)** Heat maps comparing lncRNA transcripts between iPSC and MSC EVs. **(b)** Volcano plots displaying the differentially expressed transcripts between iPSC and MSC EVs.

**Supplementary Figure 5**. Statistics of lncRNA GO enrichment analysis for **(a)** iPSC vs. A549 EVs and **(b)** MSC vs. A549 EVs. Plots depict the p value/gene number for the corresponding GO term enrichment.

**Supplementary Figure 6.** RNA pulldown assay. Biotin-conjugated synthetic RNA sequences corresponding to the sequences of interest from ADIRF-AS1 and AC120498.9 were incubated with either CCF-STTG1 or MDM extract. Western blot was performed to assess the expression of different RNA binding proteins (PKR, Dicer, RIG-I).

**Supplementary Figure 7.** Cellular viability assay. SHSY5Y cells were exposed to EVs from OC43 infected cells with or without treatment of stem cell EVs. Stem cell EVs were exposed to UV(C) to inactivate EV-associated RNAs. **(a)** Representative images show the appearance and morphology of cells after 8 days in culture. Scale bar = 200 µm. **(b)** Cell viability was quantified via CellTiter-Glo. n=3. *$p < 0.05$ ; ***$p < 0.0001$.

**Supplementary Figure 8.** iPSC EV-associated lncRNAs were sorted based on their corresponding FPKM values (FPKM ≥ 2 relative to MSC and A549 EV-associated lncRNAs). The secondary structures of these lncRNAs were predicted by the RNAfold Server of the ViennaRNA Websuite. Out of approximately 244 lncRNAs, 42 were found to contain multiple circular loops and rings. The secondary structures of those 42 lncRNAs are shown.

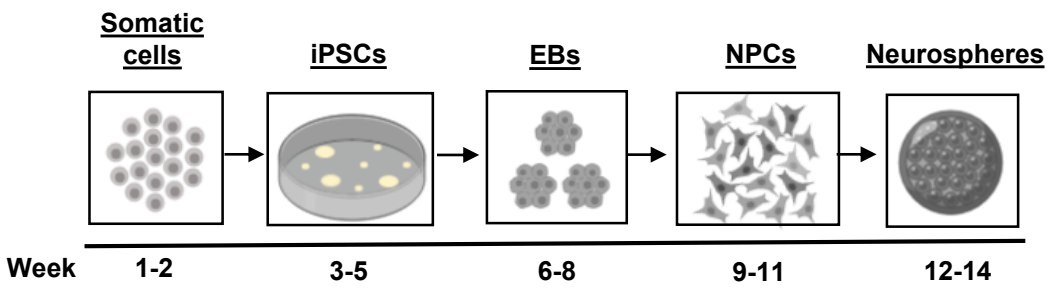


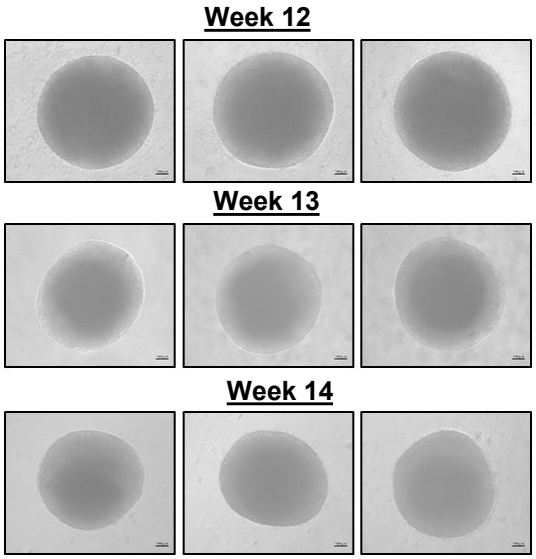


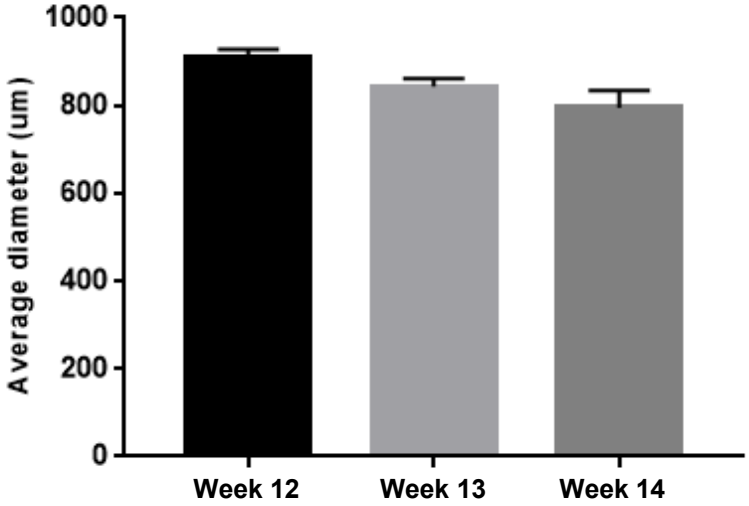


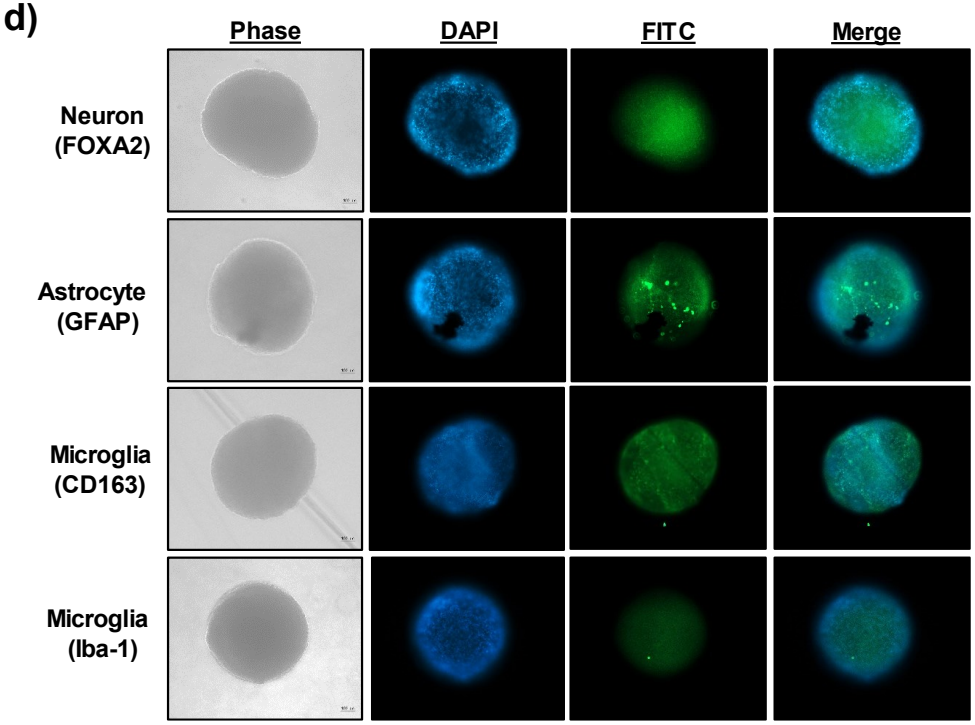


**Branscome et al. Fig. 1a-d**

a)

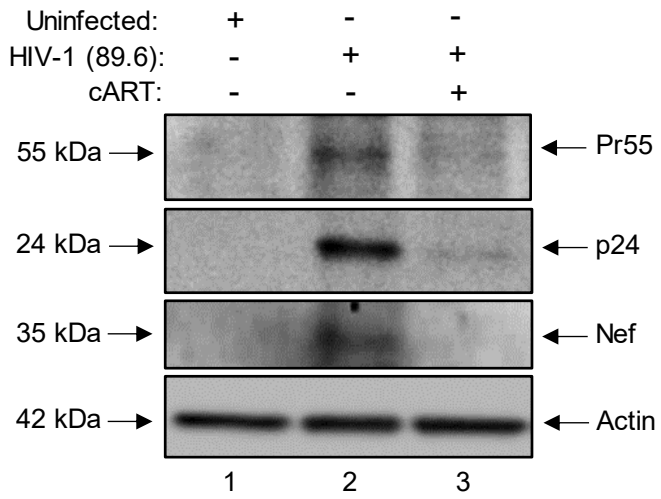


b)

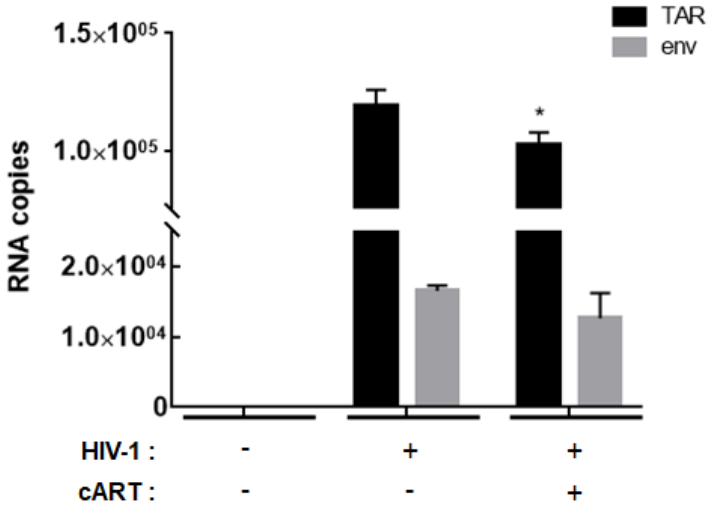


c)

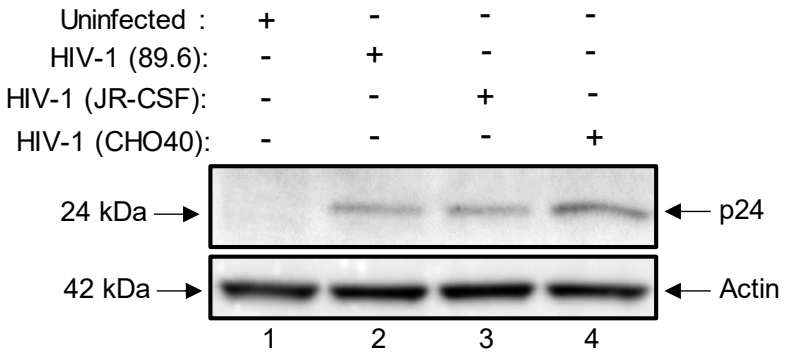


**Branscome et al. Fig. 2a-c**

d)

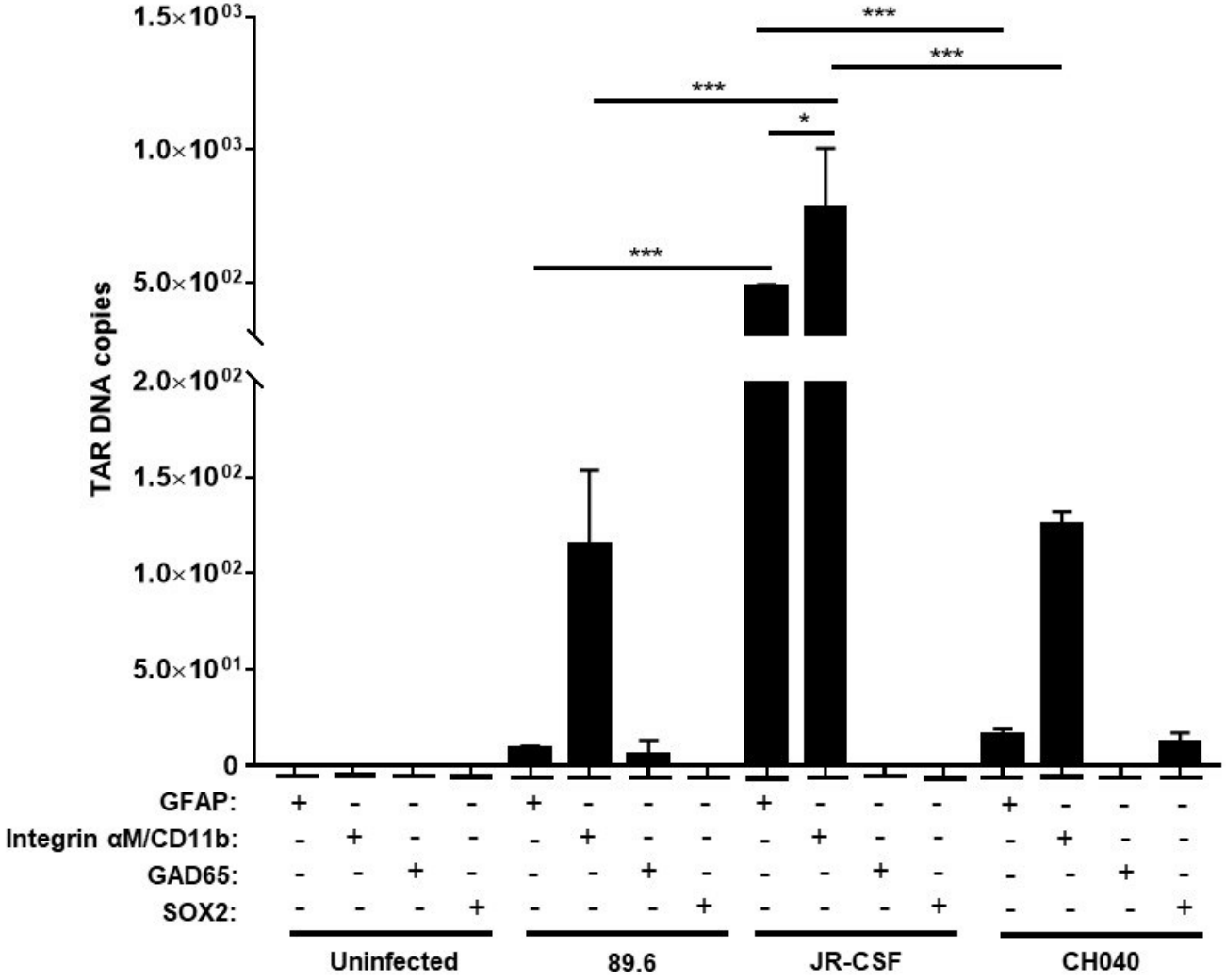


**Branscome et al. Fig. 2d**

a)

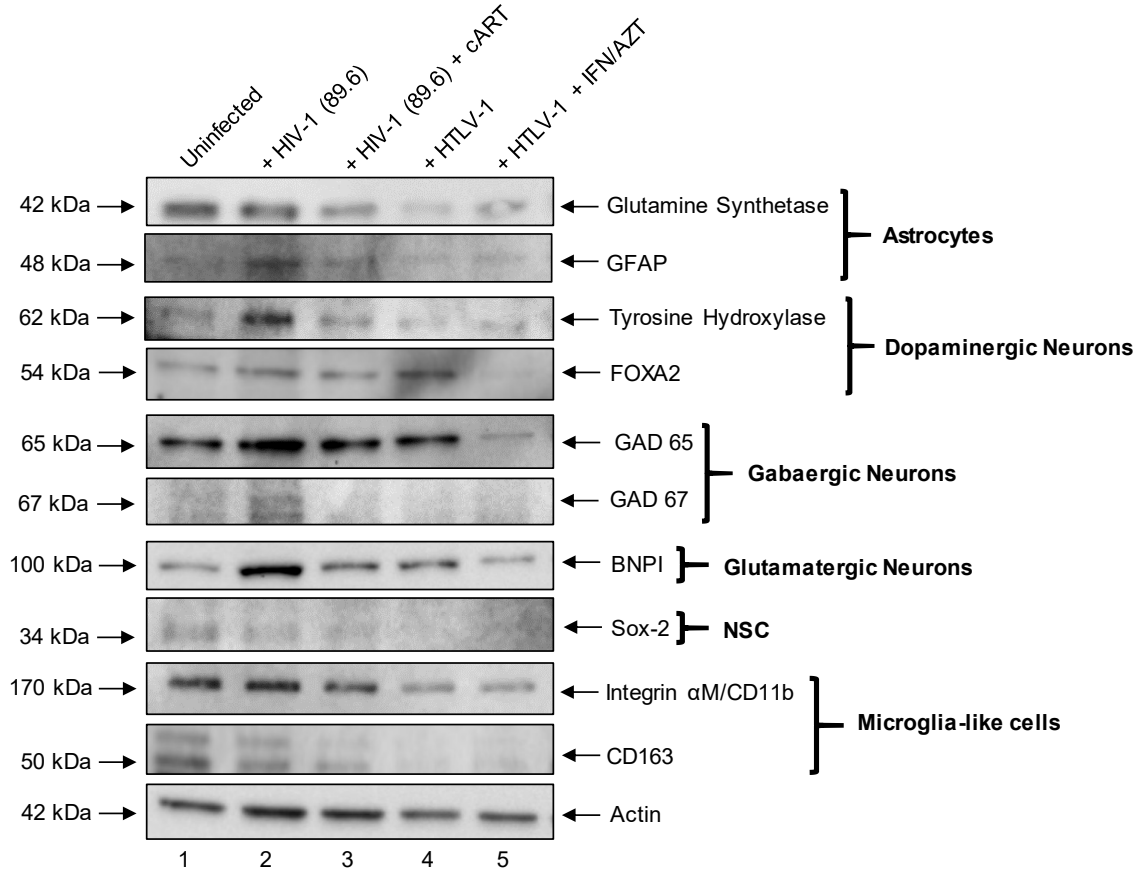


**Branscome et al. Fig. 3a**

b)

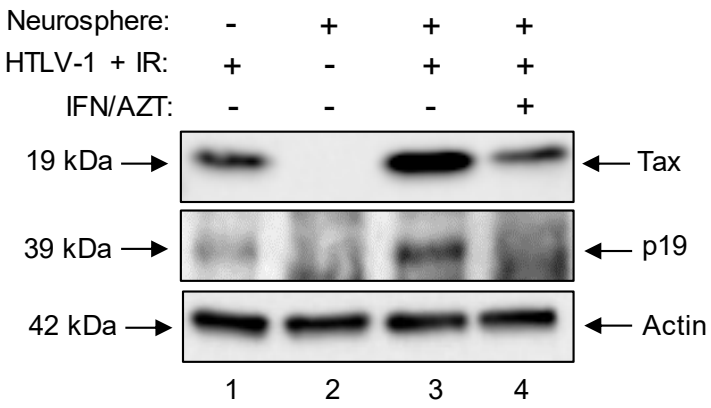


c)

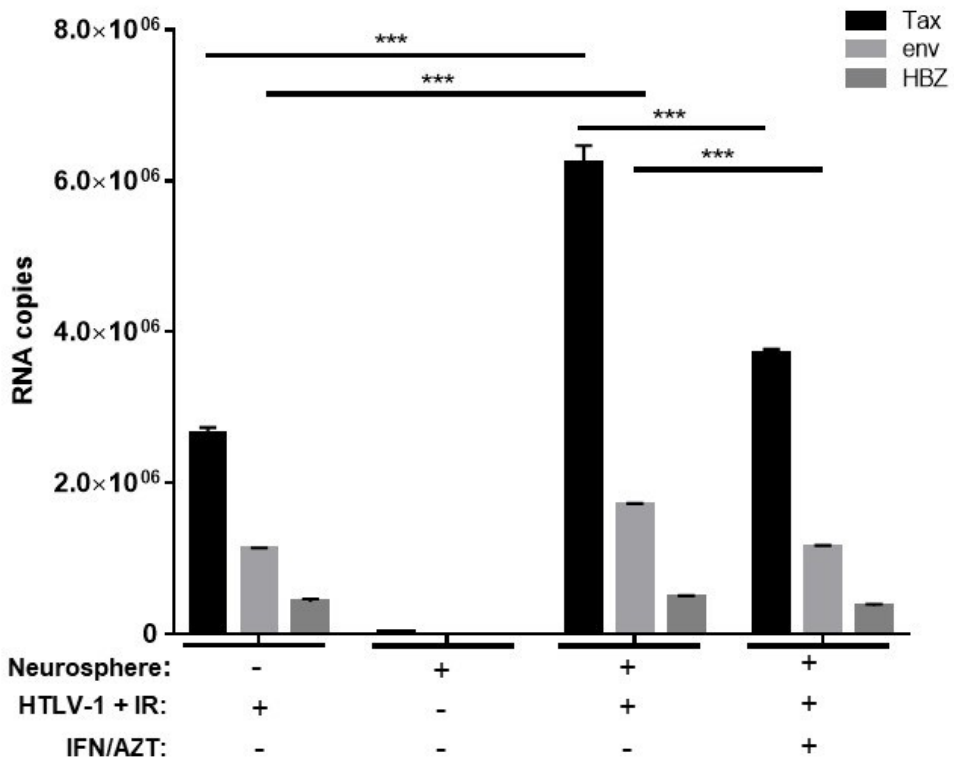


**Branscome et al. Fig. 3b-c**

a)

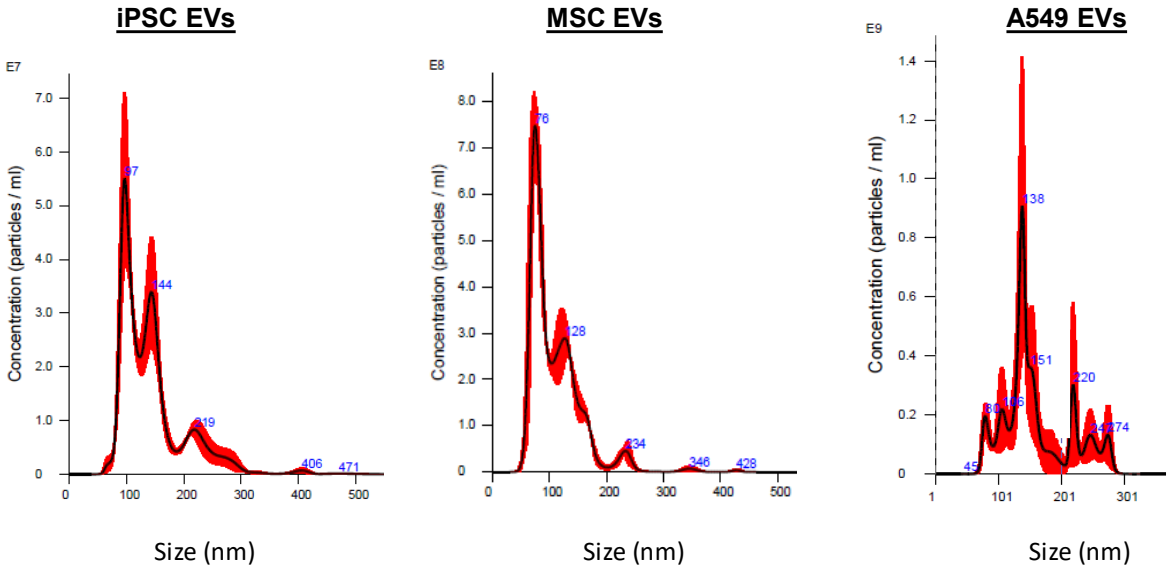


b)

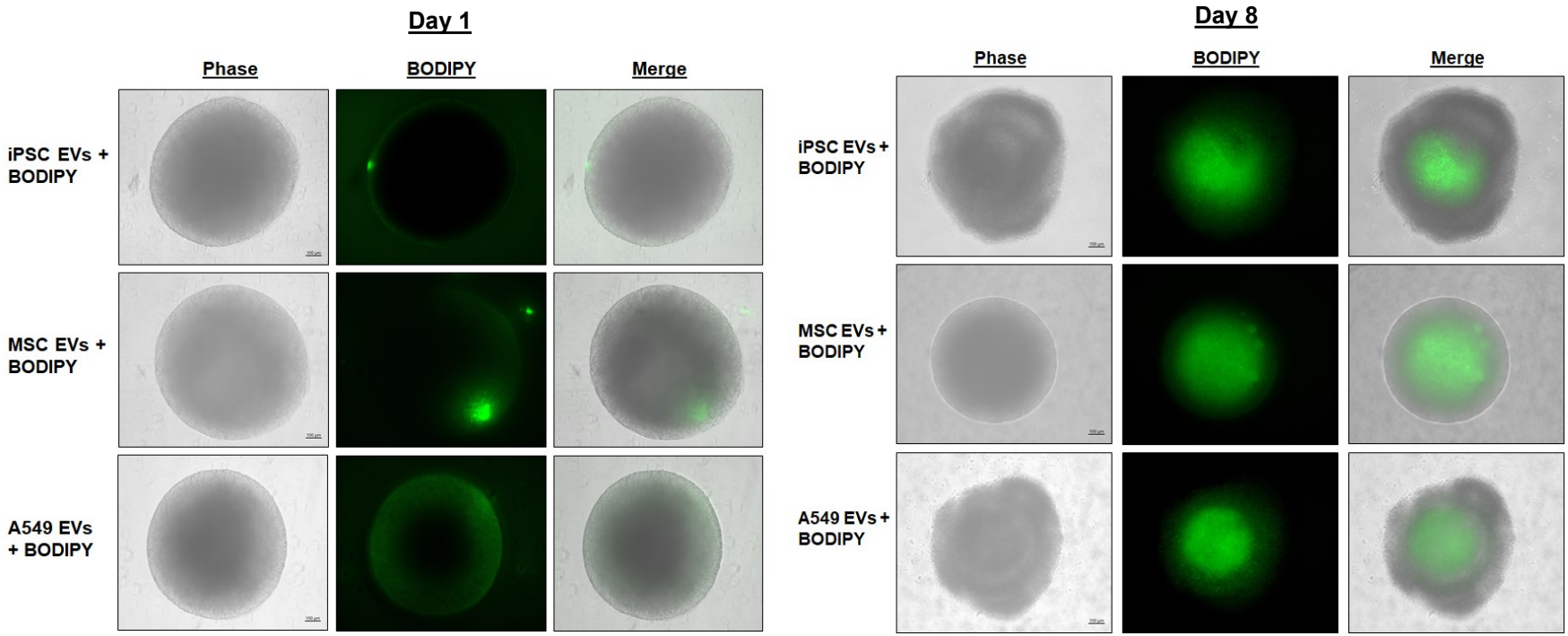


**Branscome et al. Fig. 4a-b**

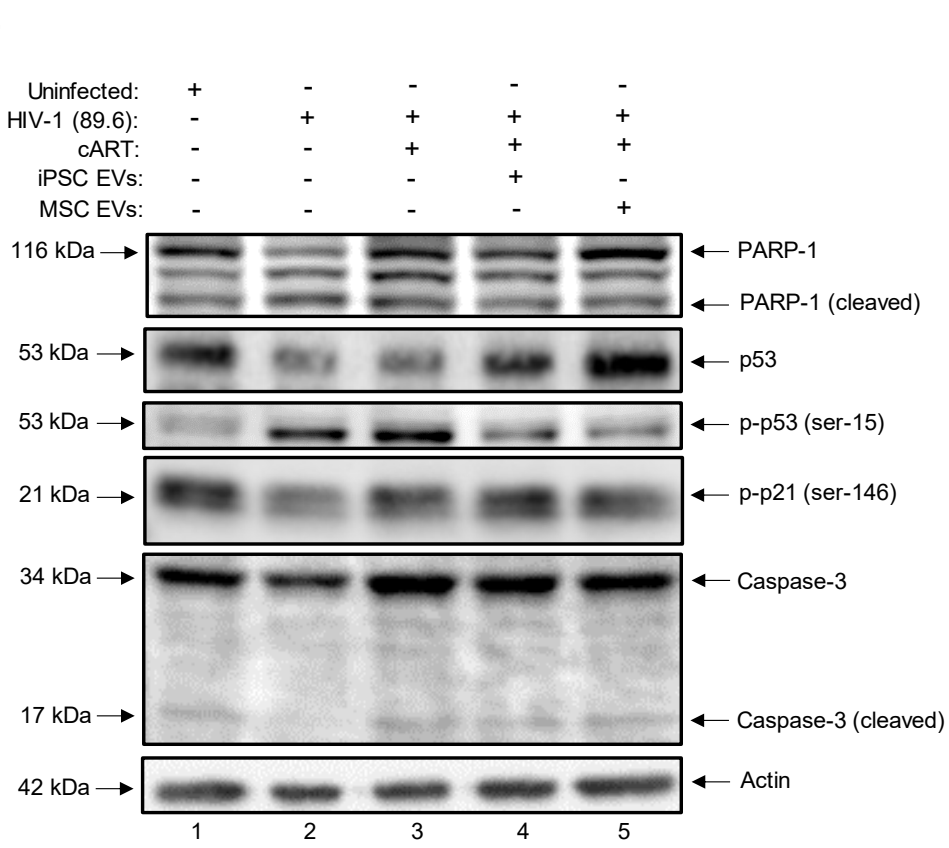


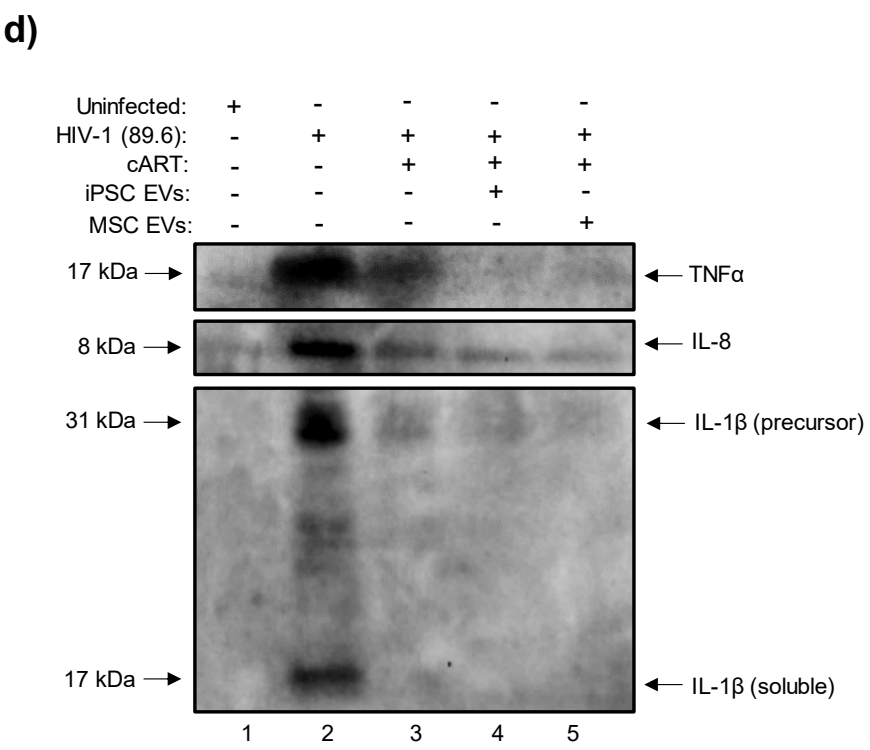


**Branscome et al. Fig. 4c-d**

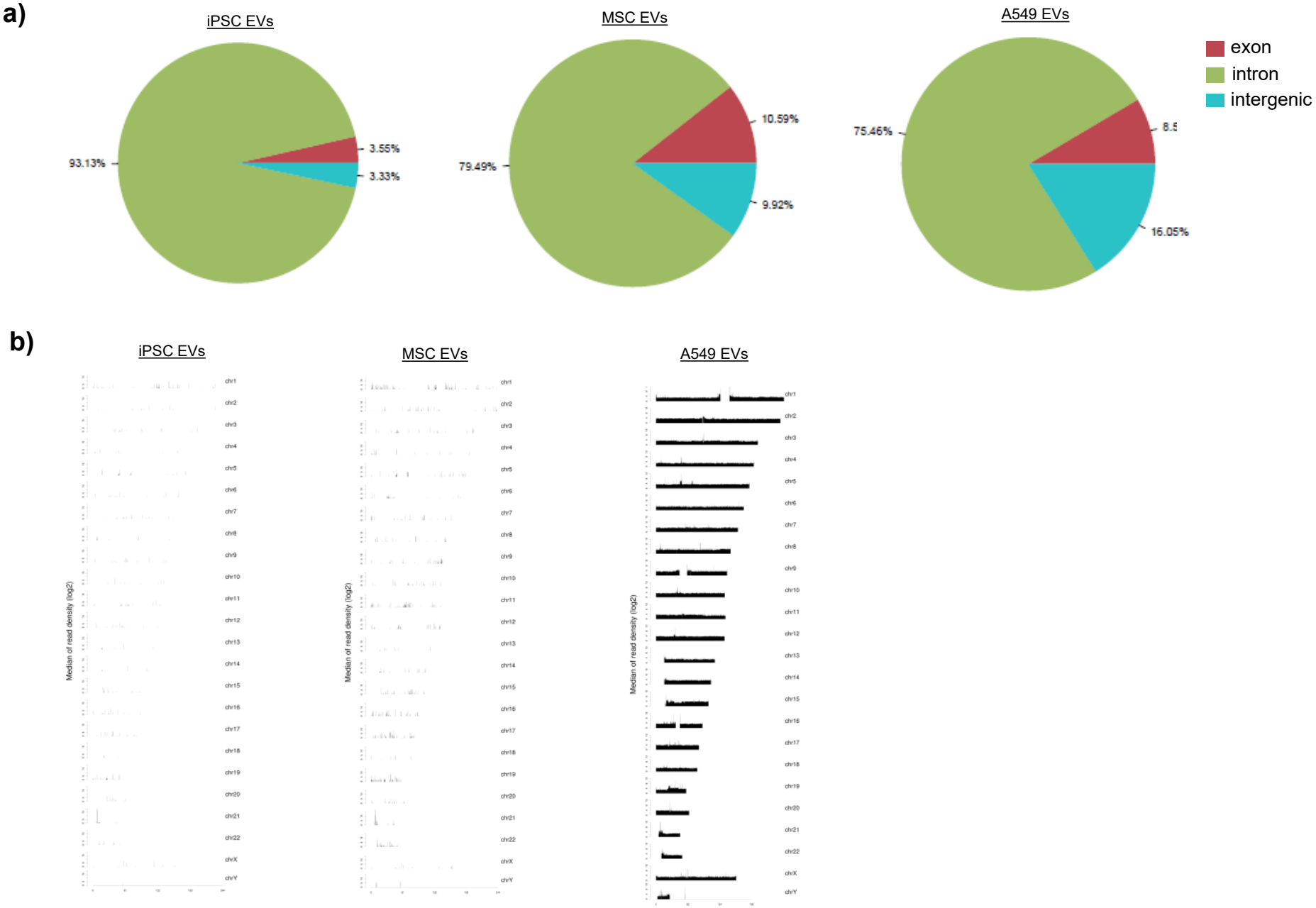


**Branscome et al. Fig. 5a-b**

c)

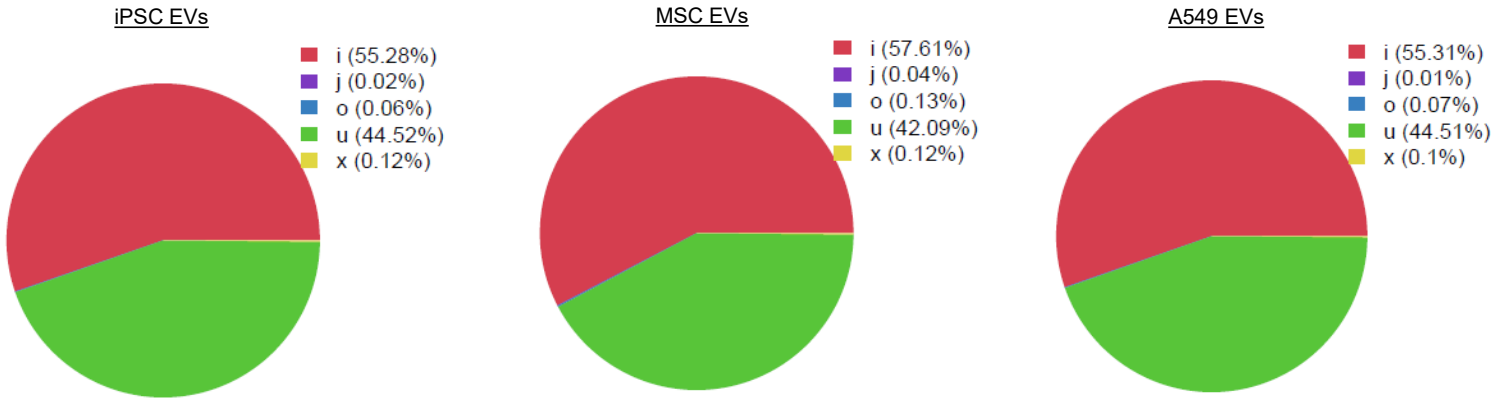


d)

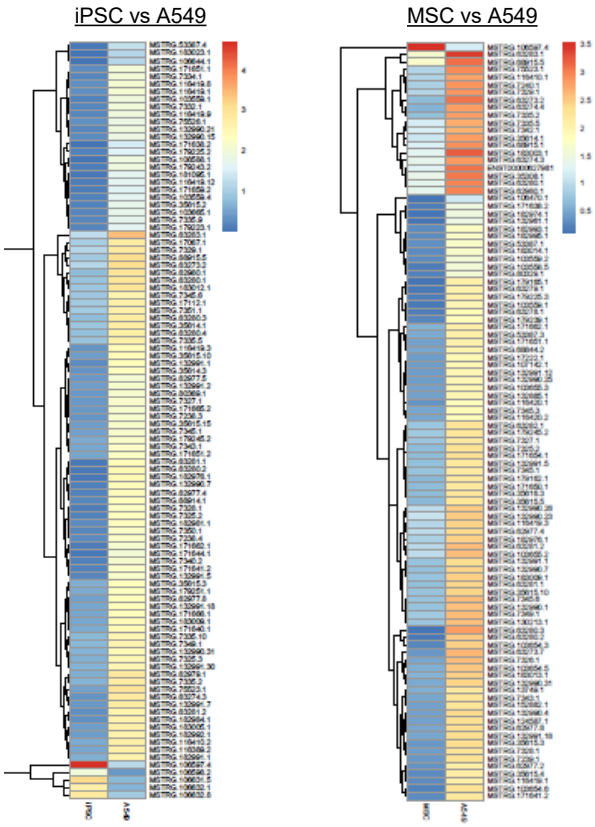


**Branscome et al. Fig. 5c-d**

e)

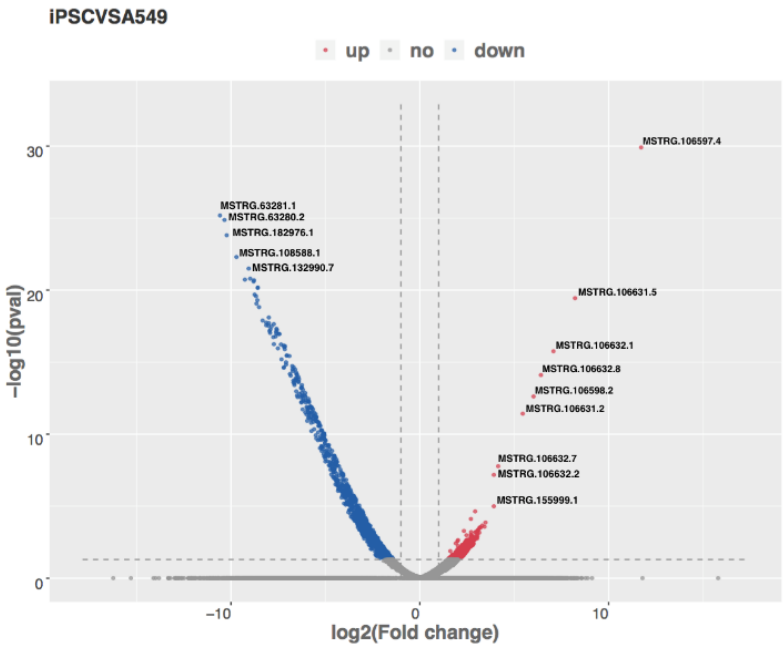


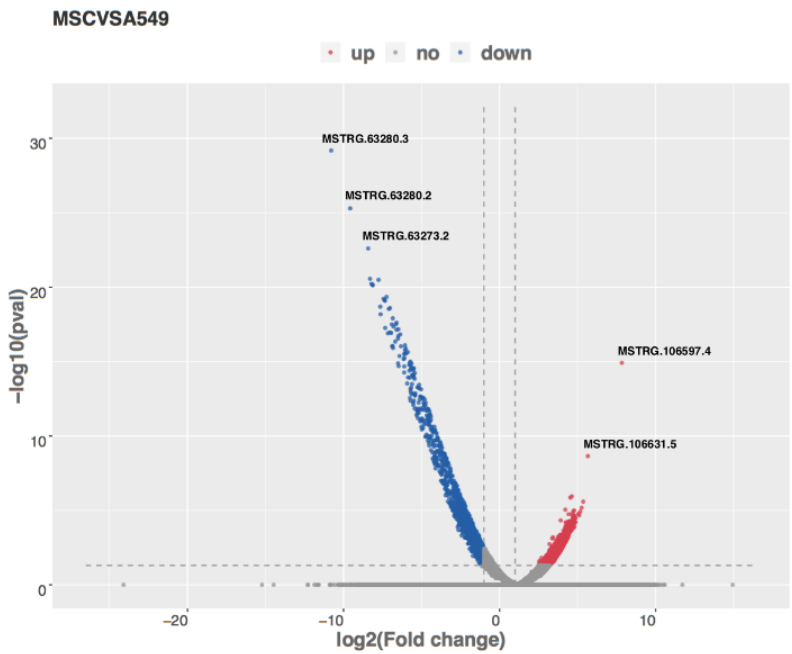


**Branscome et al. Fig. 5e**

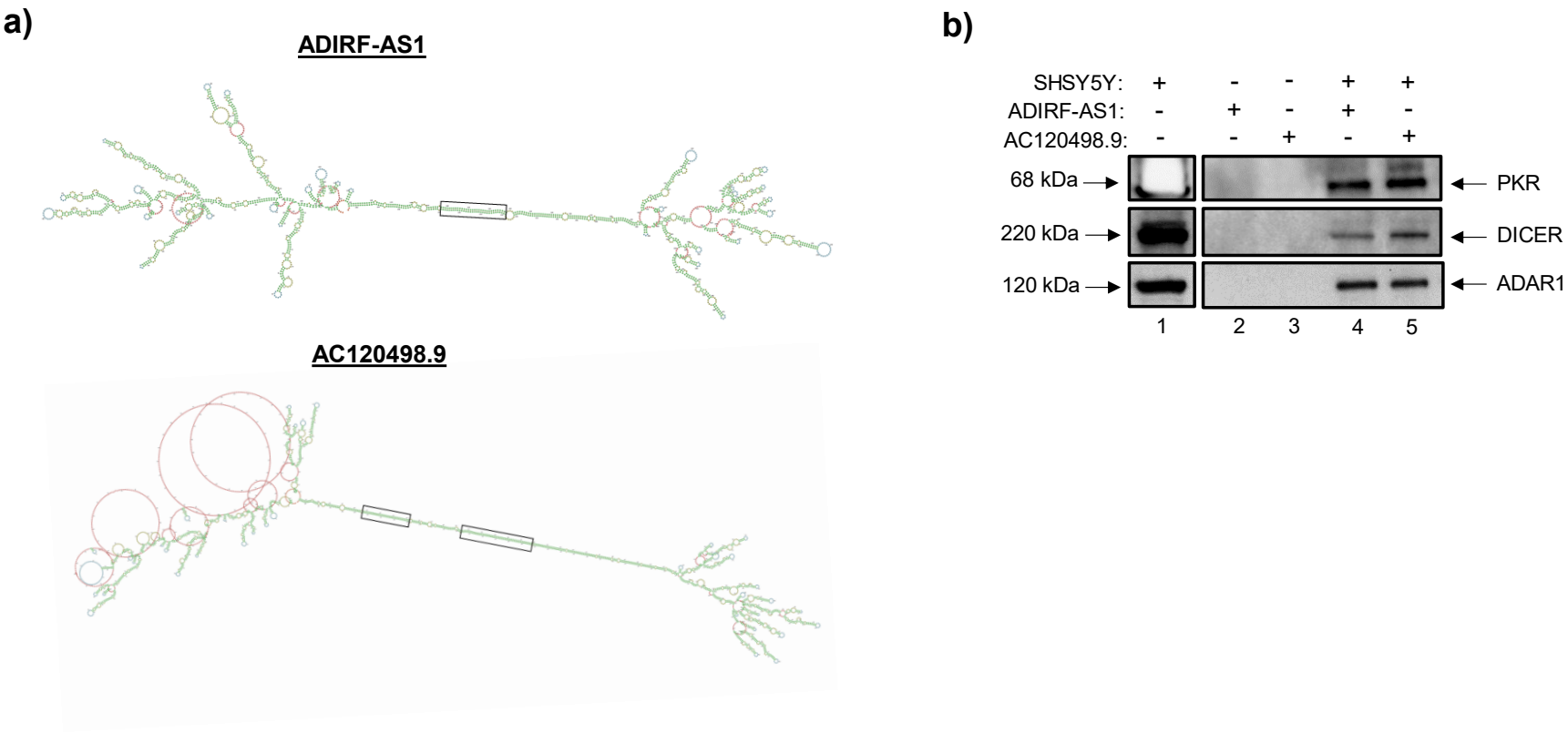


**Branscome et al. Fig. 6a-b**

c)

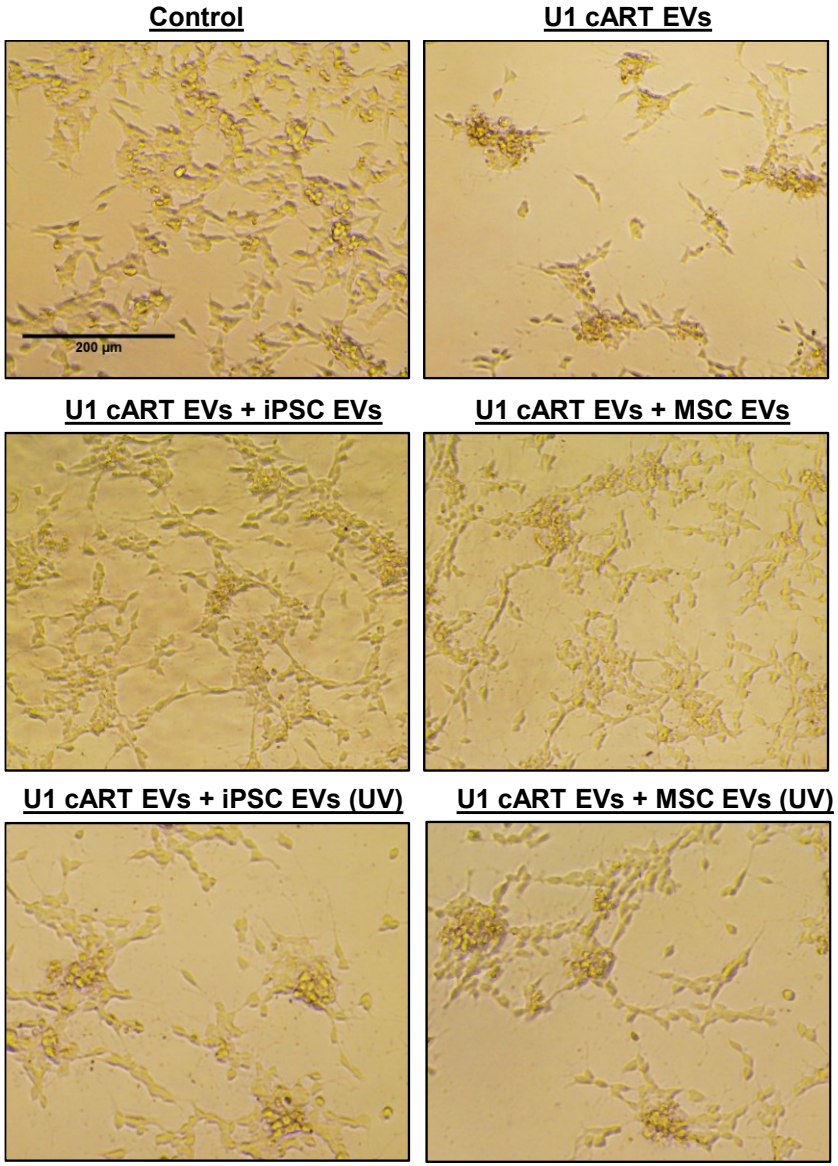


d)

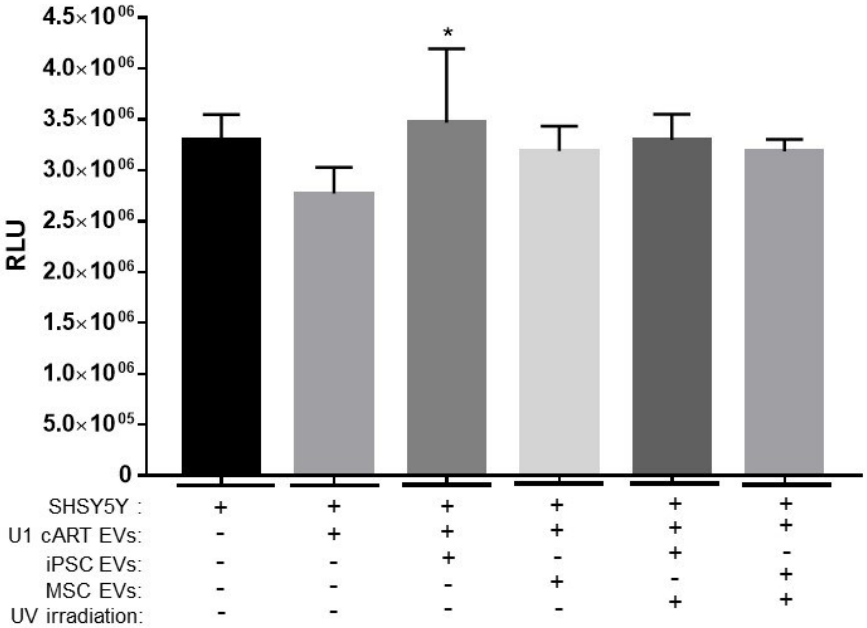


**Branscome et al. Fig. 6c-d**